SAND2007-0643J

HETEROGENEOUS DEFORMATION AND SPALL OF AN EXTRUDED TUNGSTEN ALLOY: PLATE IMPACT EXPERIMENTS AND CRYSTAL PLASTICITY MODELING

T. J. Vogler
Solid Dynamics and Energetic Materials Department
Sandia National Laboratories
Albuquerque, NM 87185-1181

J. D. Clayton
Impact Physics Branch
U.S. Army Research Laboratory
Aberdeen Proving Ground, MD 21005-5069

Abstract

The role of microstructure in the dynamic deformation and fracture of a dual phase, polycrystalline tungsten alloy under high-rate impact loading is investigated via experiments and modeling. The material of study consists of pure tungsten crystals embedded in a ductile binder alloy comprised of tungsten, nickel, and iron. The tungsten crystals are elongated in a preferred direction of extrusion during processing. Normal plate impact tests are conducted on samples oriented either perpendicular or parallel to the extrusion direction. Spatially-resolved interferometric data from these tests are used to extract wave propagation behavior and spall strength dependent upon position in the sample microstructure. Finite element simulations of impact and spall in realistically reproduced microstructures are conducted in parallel with the experiments. Finite deformation crystal plasticity theory describes the behavior of the pure tungsten and binder phases, and a stress- and temperature-based cohesive zone model captures fracture at grain and phase boundaries in the microstructure. In results from both experiments and modeling, the grain orientations affect the free surface velocity profile and spall strength statistics. Some aspects of distributions of free surface velocity and spall strength among different microstructure configurations are qualitatively similar between experimental and numerical results, while others are not as a result of differing scales of resolution and modeling assumptions. Following a comparison of experimental and numerical results for different microstructures, intergranular fracture is identified as an important mechanism underlying the spall event.

Keywords: A. Microstructures; B. Crystal plasticity; C. Plate impact; C. Finite elements; C. Probability and statistics.

1. Introduction

The response of solid materials to impact or shock loading conditions is of interest for a variety of applications, including structural crashworthiness, ballistic events, and explosive-structure interactions. Often such materials are heterogeneous when considered at the microscale; examples include polycrystalline metals and ceramics or composite systems. Here we use the terms microscale and mesoscale somewhat interchangeably, as both are encountered in the literature to describe the physics and mechanics of deformation at the scale of material features such as individual grains or particles, which can occur over 10^{-7}-10^{-2} m. For most metals and ceramics, the mesoscale is identified with the grain size, typically on the order of 10^{-6}-10^{-4} m. The microstructure has been experimentally observed to affect shock wave propagation and material failure in various solids in a number of instances (cf. Asay and Barker, 1974; Asay and Chhabildas, 2003; Brannon et al., 1983; Mescheryakov, 2003). Even so, the mesoscale remains difficult to probe experimentally in shock experiments due to the short time scales involved for stress waves to traverse individual grains. Early modeling efforts (e.g. Meyers and Carvalho, 1976) pointed toward heterogeneous shock propagation phenomena controlled by the mesoscale, but only recently has it been possible to computationally address realistic microstructures, with dimensions of several hundred microns, with advanced crystal mechanics-based constitutive models for nonlinear elastic-plastic behavior at the grain scale.

1.1 Background: experimental methods

Velocity interferometry has long been an important tool in shock physics research with the velocity interferometer system for any reflector (VISAR) (Barker, 2000) system and Fabry-Perot (McMillan et al., 1988) velocimeter being the most widely used. Bloomquist and Sheffield (1983) developed the optically recording velocity interferometer system (ORVIS) in which the photodetectors of a VISAR system are replaced by a streak camera. Their objective, though, was improved temporal resolution, and they did not consider spatially resolved phenomena. Baumung et al. (Baumung et al., 1996) made improvements to the system to allow use of a more modest laser and to allow many measurements across the width of the line. The current system, referred to as the line-VISAR, is an improved version of that of Baumung et al. and is described in Trott et al. (2001). Additional references relating to efforts towards spatially resolved velocity measurements in dynamic experiments can also be found therein. The length of the line imaged by the system can be varied from less than a millimeter to tens of millimeters by changing the optics, though in principle there is no maximum length of the line. The line-VISAR represents a significant advance over other diagnostics because it can be used to study spatially-varying phenomena, whether they arise due to multidimensional effects or material heterogeneity.

The line-VISAR has been utilized in the study of a variety of physical phenomena at the mesoscale for a number of different classes of materials. Dynamic loading of well-ordered lattices of tin spheres (Baer and Trott, 2004) and preformed ceramic lattice (Trott et al., 2007), yielding, spall, void growth, and edge release in tantalum (Chhabildas et al., 2002; Furnish et al., 2006), collapse of holes in copper samples (Furnish et al., 2004), failure of glued and welded joints (Furnish et al., 2004), edge release in sapphire (Reinhart et al., 2002), and compaction of granular sugar (Trott et al., 2006) have all been investigated. The line-VISAR has also been used to probe the shock response of fused silica, foam, glass-reinforced polyester (Trott et al., 2000), boron carbide (Vogler et al., 2004), and HMX (Baer and Trott, 2005). Laser-driven flyers have also been incorporated in such studies (Trott and Asay, 1998).

Although the line-VISAR has been used as a diagnostic for several different types of

experiments, in general it has been used to assess phenomena qualitatively rather than quantitatively. However, in a few instances line-VISAR data have been analyzed directly to determine edge release velocities (Furnish et al., 2006; Reinhart et al., 2002), void growth (Chhabildas et al., 2002), and spatial variability in the Hugoniot elastic limit (HEL) and spall strength (Furnish et al., 2006).

1.2 Background: modeling techniques

Crystal plasticity models capturing anisotropy arising from individual slip system activity have been used to describe deformation of metallic materials for some time (see, e.g. Asaro, 1983; Kocks et al., 1998). Historically, most crystal plasticity implementations have focused on the quasi-static loading regime, though models have been applied in the intermediate strain rate regime to address dynamic phenomena such as those occurring in Hopkinson bar experiments (Nemat-Nasser et al., 1998), Taylor impact experiments (Schoenfeld, 1998), explosive forming of polycrystalline tantalum liners (Schoenfeld, 1998), and ballistic impact of titanium armor plates (Schoenfeld and Kad, 2002).

Recently, the crystal plasticity approach with resolution of individual grains by many finite elements has been applied to model the very high-rate (shock) loading regime (Becker, 2004; Clayton, 2005b). Simulations in this regime are often more computationally intensive than for quasi-static loading because the former require (i) refined meshes needed to resolve stress waves, shock fronts, and material instabilities, and (ii) explicit integration methods for the equations of motion requiring very small time increments for numerical stability. In particular, Becker's (2004) simulations of polycrystalline tantalum demonstrated heterogeneities of stress and deformation at the grain scale, and shock fronts whose roughness decreased significantly as the applied stress rose from 10 to 100 GPa. Becker also pointed out the presence of nonuniformities in the free-surface velocity that would complicate interferometric velocity measurements in analogous plate impact experiments. It is precisely these variations that are the focus of the current investigation.

Spall fracture and wave propagation in polycrystalline ceramics have been studied numerically with cohesive finite elements addressing fracture at grain boundaries (Espinosa and Zavattieri, 2003a; b). In that particular study, in which the bulk behavior was dictated by isothermal, anisotropic linear elasticity, local fracture behavior and heterogeneous wave propagation were observed. Comprehensive parametric studies with variable cohesive properties and mesh densities were the focus of the investigation, and although the simulations mimicked plate impact tests, direct comparisons with experimental data were not reported.

An alternative to the finite element method that has recently been employed to resolve the shock deformation of polycrystalline metals at the mesoscale is the discrete-element method (DEM) (Case and Horie, 2006; Yano and Horie, 1999; 2002). Simulations using this technique have, to date, been two-dimensional and utilized very simple means to account for grain-to-grain variations in behavior, specifically orientation-dependent HELs, elastic wave speeds, and plastic wave speeds. Nonetheless, the aforementioned DEM models have been exercised to display a rich set of physically realistic behaviors including a non-uniform shock front, lateral motion near the shock, and vortices in material motion.

In most of the cases cited above, few comparisons were between simulation results and experimental data on behavior at the mesoscale, in large part because of a lack of available experimental data in that spatial regime. In a few cases, line-VISAR results have been compared to numerical simulations of the dynamic loading of granular sugar packings (Trott et al., 2006)

and ordered packings of tin spheres (Baer and Trott, 2004). These have been large-scale three-dimensional numerical simulations conducted with Eulerian hydrocodes, as opposed to Lagrangian FEM or DEM. Furthermore, these simulations have historically focused on the effects engendered by variations in spatial distributions of spherical or cubic particles in regular or random arrays, in the context of relatively simple isotropic elastic or elastic-plastic constitutive theories for the deviatoric response. In these instances, comparison between the simulations and experimental results have generally focused on comparing the average response or homogenized material properties.

1.3 Background: tungsten alloys

Tungsten heavy alloys (WHA) such as the one studied here have been investigated for decades, primarily as potential materials for kinetic energy projectiles (Bless et al., 2006; Magness, 1994). Mechanical properties and physical phenomena at high strain rates have been obtained or observed using Hopkinson bar techniques (Kim et al., 1998; Ramesh and Coates, 1992; Weerasooriya and Beaulieu, 1993), normal plate impact (Bless and Chau, 2006; Dandekar and Weisgerber, 1999; Millett et al., 1999; Zurek and Gray, 1991), explosive loading (Baoping et al., 1994), and oblique flyer-plate impact (Zhou and Clifton, 1997). In many of these cases, the bulk mechanical properties of the homogenized multi-phase material (e.g. stress-strain curves, Hugoniot data, and spall strengths) were of primary interest, though some effects of local behavior dominated by microstructure, such as fracture surfaces or shear localization initiation sites, have been reported and described.

The role of microstructure on dynamic mechanical properties of tungsten alloys has also been investigated via constitutive modeling and numerical simulation. Zhou and co-workers used an isotropic elastic-viscoplastic constitutive model with realistic grain structures to capture shear localization in oblique impact (pressure-shear conditions) (Zhou et al., 1994) and high-rate nominally uniform shear deformation (Zhou, 1998b). Effects of microstructural properties (thermal conductivity and temperature-dependent flow stress) on shear band formation in pressure-shear were also studied numerically (Zhou, 1998a). Batra and Love (2006a; 2006b) studied adiabatic shear bands in tungsten composites deformed in plane strain tension, and fracture in functionally graded tungsten composites using a nodal release method (Batra and Love, 2005). Effective properties of tungsten alloys depending on microstructural parameters (e.g. volume fraction, size, and distribution of pure tungsten grains) were also determined numerically (Love and Batra, 2005).

The above modeling studies incorporated isotropic constitutive models for pure tungsten, a body-centered cubic (BCC) material whose single crystals are virtually elastically isotropic at low pressures (Hirth and Lothe, 1982) yet are known to exhibit significant anisotropy with regards to plastic flow (Argon and Maloof, 1966; Subhash et al., 1994). To address the effects of crystallographic orientation and dislocation accumulation on the thermomechanical response of tungsten alloys, crystal plasticity-based constitutive models have recently been formulated and implemented by one of the authors. Tensile deformation and fracture of realistically rendered (Clayton, 2005a) and homogenized (Clayton, 2006a) microstructures of dual phase tungsten alloys have been studied, respectively, with cohesive zone and anisotropic continuum damage mechanics theories. Clayton (2005b) performed two-dimensional simulations of high-rate, uniaxial strain compression and spall fracture of a two-phase tungsten heavy alloy. It was found that grain shapes and orientations had a significant effect on the nature of propagating stress waves, while spall was influenced by both of these aspects as well as by the local interfacial

properties used in the model. Statistical variations of free surface velocity were also found to vary with crystal orientation, texture, and temperature dependence of properties controlling grain boundary fracture (Clayton, 2006b).

1.4 Objectives and scope

In this paper, results are presented for planar impact experiments on WHA in conjunction with new results from simulations obtained using the crystal plasticity-cohesive fracture modeling methods developed by Clayton (2005b). The line-VISAR utilized in the experiments provides spatially- and temporally-resolved data on material deformation. It also provides statistical information regarding the local spall strength of the material. Aspects of the material response not reported in previous modeling of impact (Clayton, 2005b; 2006b) are analyzed here, including different impact velocities and variations in orientations of extruded grain structures (i.e., elongated grains oriented perpendicular or parallel to the compression wave). In parallel, effects due to sample orientation and impact velocity are explored in plate impact experiments.

Although comparison between experiments and simulations is not straightforward at present due to competing limitations on the spatial resolution of the experimental system and the absolute size of the computational domain, there are aspects of the two that can be compared in a meaningful way. For example, it is possible to compare trends observed in experimental results with those from the simulations such as the effect of microstructural orientation on average spall strength. Changes in free surface velocities and corresponding statistics of the response with increasing impact velocity or changes in sample orientation can be compared between model and experiment. For example, changes in variance of free surface velocity with changes in grain orientation may or may not be reflected by either the experiments or the simulations. Further, the capability for the simulations to detect features of the experimental results, such as characteristic spikes in velocity dispersion through the shock front (cf. Case and Horie, 2006), provides an important means assess the validity of the simulations. In this way, experiments enable validation and possible improvement of crystal elasticity and plasticity models for high-rate applications, and simulations offer explanations and insight into macroscopic and mesoscopic aspects of material behavior-- either observed or predicted--that are difficult to resolve or deduce through experiments alone. This work represents a crucial first step toward developing meaningful ways to compare the two sets of results.

The paper is organized as follows: experimental methods, modeling methods, experimental results, modeling results, discussion, and conclusions. Cartesian coordinates are used, with summation implied over repeated indices. Vector and tensor quantities are represented with boldface type, while scalars and individual components of vectors and tensors are written in italics. Juxtaposition implies summation over two repeated adjacent indices (e.g. $\left(\mathbf{AB}\right)_a^b = A_{ac}B^{cb}$). The dot (scalar) product of vectors is represented by the symbol "•" (e.g. $\mathbf{a}\bullet\mathbf{b} = a^a b_a$). The colon denotes contraction over repeated pairs of indices (e.g. $\mathbf{A}:\mathbf{B} = tr\left(\mathbf{A}^T\mathbf{B}\right) = A_{ab}B^{ab}$ and $\mathbf{C}:\mathbf{A} = C^{abcd}A_{cd}$). The symbol "$\otimes$" represents the tensor (outer) product (e.g. $\left(\mathbf{a}\otimes\mathbf{b}\right)^{ab} = a^a b^b$). Superposed -1, T, and "•" denote inverse, transpose, and material time derivative operations, respectively. Additional notation is explained as it appears.

2. Experimental approach

The tungsten alloy studied consists of grains of relatively brittle pure tungsten (BCC) in a relatively soft and ductile face centered cubic (FCC) matrix composed of nickel (50% by weight), iron (25%), and tungsten (25%) as shown in Fig. 1. The alloy nominally consists of 90% tungsten grains and 10% matrix alloy, yielding an overall mass composition of 93W-5Ni-2Fe. The composite is fabricated through isostatic pressing and sintering of a mixture of W, Ni, and Fe powders. The alloy is then annealed to remove absorbed hydrogen and may be quenched, swaged, or pre-twisted to enhance its dynamic properties. Typical grain sizes are 10-30 μm for the W crystals and 200-500 μm for the matrix phase, implying that each matrix grain contains several W grains. The average density of the material was found to be 17.77 ± 0.07 g/cm^3.

As a result of the swaging process, the W grains are elongated in the direction of the axis of the kinetic energy (KE) rod from which material was obtained. As a means to assess the effect of the microstructure on shock wave propagation and spall failure, thin plates with two orientations were tested. The first, shown as a disk Fig. 2 and referred to as the axial orientation, aligns the sample normal with the axis of the rod, giving elongated W grains through the sample thickness as shown in the electron backscatter diffraction (EBSD) image in the upper left. The second, shown as a thin square sample in Fig. 2 and referred to as the transverse orientation, has a sample normal that is perpendicular to the axis of the rod. For these samples, two edges show equiaxed grains as shown in the upper right EBSD image, while the other two reveal the elongated grains of the upper left EBSD image. The line-VISAR was thus oriented with respect to the grains as illustrated in Fig. 2 in order to account for in-plane anisotropy of the sample. Despite the orientation dependence of the composite microstructure, the homogenized material is essentially elastically isotropic at the macroscale, with longitudinal and shear wave speeds of 5.19 and 2.83 km/s, respectively. Note that pure tungsten is an unusual cubic material in the sense that its single crystals are elastically isotropic at low pressures (Hirth and Lothe, 1982), though deviations from elastic isotropy and phase transformations occur at very high pressures (Ruoff et al., 1998). Hence, any deviations from elastic isotropy in the WHA are caused by finite deformations or the presence and distribution of the presumably anisotropic binder phase, as well as local lattice imperfections such as grain, twin, or subgrain boundaries.

Five plate impact experiments were performed. A compressed gas gun was used to launch a 1.5 mm thick WHA impactor into a 3.0 mm thick WHA target at velocities of approximately 250, 350, and 450 m/s. Two samples exhibited the axial orientation and the other three were transversely oriented. All impactors had axial orientation. Details for the five experiments are given in Table 1, and a schematic of the experimental setup is shown in Fig. 3. The WHA impactor was mounted on a TPX (polymethylpentene) layer to give a nearly complete unloading, and that in turn was mounted on the front of an aluminum projectile. Projectile velocities were measured to better than 0.5% by means of three shorting pins of different heights, and tilts were determined through four pins distributed around the circumference of the sample. In all cases except experiment WHA-5 the tilt was less than 0.5 milliradians. In experiment WHA-5, it appears that there was separation of the WHA impactor from the projectile sometime prior to impact since the tilt pins indicated only a small tilt but the line-VISAR streaks indicated significant tilt. Also, the impactor may not have been entirely planar, perhaps due to bowing. The back surface of the target was diamond turned and then diffused with glass beads to facilitate good reflectance for the line-VISAR system used to monitor the velocity. Following the experiment, debris was collected for metallographic analysis, which will be reported separately in the future. It should be noted that no special precautions were taken to ensure

"soft" recovery of the sample since it will inevitably strike the reflecting mirror of the line-VISAR.

3. Modeling approach

Essential features of the constitutive models for tungsten and binder phases are given here, followed by a brief description of the cohesive fracture model used for describing failure along internal material interfaces. Descriptions of the numerical simulations are then provided. The reader is referred to (Clayton, 2005b) for further details regarding the numerical implementation, and (Clayton, 2005a; b) for theoretical and experimental justification of particular aspects of the model and selection of material parameters.

3.1 Crystal plasticity theory

A finite deformation, rate dependent crystal plasticity model is used to capture the thermomechanical behavior of the tungsten crystals and W-Ni-Fe binder phase. The same model framework, albeit with different parameters, is used for each material.

Denoted by $\mathbf{x} = \mathbf{x}(\mathbf{X},t)$ is a smooth time-dependent motion, where $\mathbf{x}$ and $\mathbf{X}$ are spatial and reference coordinates, respectively. The local deformation gradient $\mathbf{f}$ is decomposed as

$$\mathbf{f} \equiv \frac{\partial \mathbf{x}}{\partial \mathbf{X}} = \mathbf{f}^{\mathrm{e}}\mathbf{f}^{\theta}\mathbf{f}^{\mathrm{p}}, \tag{1}$$

where $\mathbf{f}^{\mathrm{e}}$, $\mathbf{f}^{\theta}$, and $\mathbf{f}^{\mathrm{p}}$ denote the kinematics of elasticity and rigid-body rotation, stress-free thermal expansion or contraction, and the cumulative contribution of moving crystal defects such as dislocations and deformation twins. The slip direction vectors $\mathbf{s}^{(\alpha)}$ and slip plane normal vectors $\mathbf{m}^{(\alpha)}$ stretch and rotate from their respective reference representations $\mathbf{s}_0^{(\alpha)}$ and $\mathbf{m}_0^{(\alpha)}$ via thermoelastic deformation as

$$\mathbf{s}^{(\alpha)} = \mathbf{f}^{\mathrm{e}}\mathbf{f}^{\theta}\mathbf{s}_0^{(\alpha)}, \qquad \mathbf{m}^{(\alpha)} = \mathbf{m}_0^{(\alpha)}\mathbf{f}^{\theta-1}\mathbf{f}^{\mathrm{e}-1}. \tag{2}$$

The spatial velocity gradient $\mathbf{l}$ may be split additively as

$$\mathbf{l} \equiv \frac{\partial \dot{\mathbf{x}}}{\partial \mathbf{x}} = \dot{\mathbf{f}}\mathbf{f}^{-1} = \underbrace{\dot{\mathbf{f}}^{\mathrm{e}}\mathbf{f}^{\mathrm{e}-1}}_{\equiv \mathbf{l}^{\mathrm{e}}} + \underbrace{\mathbf{f}^{\mathrm{e}}\dot{\mathbf{f}}^{\theta}\mathbf{f}^{\theta-1}\mathbf{f}^{\mathrm{e}-1}}_{\equiv \mathbf{l}^{\theta}} + \underbrace{\mathbf{f}^{\mathrm{e}}\mathbf{f}^{\theta}\dot{\mathbf{f}}^{\mathrm{p}}\mathbf{f}^{\mathrm{p}-1}\mathbf{f}^{\theta-1}\mathbf{f}^{\mathrm{e}-1}}_{\equiv \mathbf{l}^{\mathrm{p}}}, \tag{3}$$

with thermal deformation assumed isotropic:

$$\mathbf{l}^{\theta} = \dot{\mathbf{f}}^{\theta}\mathbf{f}^{\theta-1} = \alpha_T\dot{\theta}\mathbf{1}, \tag{4}$$

where θ is the absolute temperature and α_T is the temperature-dependent thermal expansion coefficient giving the change in length per unit current length per unit increment in θ. The unit tensor is written as $\mathbf{1}$. The plastic velocity gradient in the intermediate configuration is defined as

$$\bar{\mathbf{l}}^{\mathbf{p}} \equiv \dot{\mathbf{f}}^{\mathbf{p}}\mathbf{f}^{\mathbf{p}-1} = \sum_{\alpha=1}^{n} \dot{\gamma}^{(\alpha)} \mathbf{s}_0^{(\alpha)} \otimes \mathbf{m}_0^{(\alpha)}, \tag{5}$$

with $\dot{\gamma}^{(\alpha)}$ the plastic shearing rate on slip system α, and n the number of potentially active slip systems.

Local balance laws in the spatial configuration are

$$\dot{\rho} + \rho\, tr\left(\mathbf{l}\right) = 0, \qquad div\boldsymbol{\sigma} + \rho\mathbf{b} = \rho\ddot{\mathbf{x}}, \qquad \boldsymbol{\sigma} = \boldsymbol{\sigma}^{T}, \qquad \rho\dot{e} + div\mathbf{q} = tr(\boldsymbol{\sigma}\mathbf{l}), \tag{6}$$

with ρ, $\boldsymbol{\sigma}$, $\mathbf{b}$, e, and $\mathbf{q}$ denoting the current mass density, Cauchy stress tensor, body force vector per unit mass, internal energy per unit mass, and heat flux vector per unit current area, respectively. The local entropy inequality is written as

$$\rho\dot{\eta} \geq -div\left(\mathbf{q}/\theta\right), \tag{7}$$

with $\dot{\eta}$ the time rate of entropy production per unit mass and *div* the spatial divergence. The Helmholtz free energy per unit mass is defined as

$$\psi \equiv e - \theta\eta, \tag{8}$$

and is assumed to be of the functional form

$$\psi = \psi\left(\mathbf{e}^{\mathbf{e}}, \theta, \xi\right), \tag{9}$$

where the intermediate configuration elastic strain $2\mathbf{e}^{\mathbf{e}} = \mathbf{f}^{\mathbf{e}T}\mathbf{f}^{\mathbf{e}} - \mathbf{1}$. The symbol ξ denotes a dimensionless scalar internal variable representing stored micro-elastic energy associated with crystal defects. From (6)-(9), one may deduce the following constitutive relationships:

$$\mathbf{s}^{\mathbf{e}} = \tilde{\rho}\, \partial_{\mathbf{e}^{\mathbf{e}}}\psi, \tag{10}$$

$$\eta = \alpha_{T}\, tr(\boldsymbol{\sigma}) / \rho - \partial_{\theta}\psi, \tag{11}$$

$$\sum_{\alpha=1}^{n} \tau^{(\alpha)}\dot{\gamma}^{(\alpha)} - \rho\left(\partial_{\xi}\psi\right)\dot{\xi} \geq \frac{\mathbf{q}\bullet\nabla_{\mathbf{x}}\theta}{\theta}, \tag{12}$$

where the elastic second Piola-Kirchhoff stress $\left(s^{e}\right)^{\alpha\beta} \equiv j^{e} f^{e-1\alpha}_{\ \ a}\sigma^{ab} f^{e-1\beta}_{\ \ b}$ with $j^{e} \equiv \tilde{\rho}/\rho = \det\mathbf{f}^{\mathbf{e}}$, and the resolved shear stress $\tau^{(\alpha)} \equiv \boldsymbol{\sigma} : (\mathbf{s}^{(\alpha)} \otimes \mathbf{m}^{(\alpha)})$. The spatial gradient is written as $\nabla_{\mathbf{x}}$. Isotropic heat conduction in the spatial frame is dictated by Fourier's law:

$$\mathbf{q} = -k\nabla_{\mathbf{x}}\theta, \tag{13}$$

with $k(\mathbf{x},\theta)$ the spatial thermal conductivity. Defining the specific heat capacity $\hat{c} \equiv \partial_{\theta} e$, the local energy balance (6) can be written as

$$\underbrace{\rho\hat{c}\dot{\theta}}_{\substack{\text{temperature}\\ \text{change}}} = \underbrace{\sum_{\alpha=1}^{n}\tau^{(\alpha)}\dot{\gamma}^{(\alpha)}}_{\substack{\text{plastic}\\ \text{dissipation}}} - \underbrace{\rho\left(\left(\partial_{\xi}\psi\right)-\theta\left(\partial_{\theta\xi}\psi\right)\right)\dot{\xi}}_{\substack{\text{energy of}\\ \text{lattice defects}}} + \underbrace{\rho\theta\partial_{\theta\mathbf{e}^{\mathrm{e}}}\psi:\dot{\mathbf{e}}^{\mathrm{e}}}_{\text{thermoelastic coupling}} + \underbrace{div\left(k\nabla_{\mathbf{x}}\theta\right)}_{\substack{\text{heat}\\ \text{conduction}}}. \tag{14}$$

The subsequent discussion pertains specifically to the cubic metallic materials (i.e., phases of tungsten alloy) of interest. A free energy potential per unit intermediate configuration volume is specified as

$$\tilde{\rho}\psi = K_0\left(\theta\right)\vartheta^2/2 - K_1\vartheta^3/3 + \mu\left(\theta\right)\mathbf{e}^{\mathrm{e}'}:\mathbf{e}^{\mathrm{e}'} + \kappa\mu\left(\theta\right)\xi^2/2 + z\left(\theta\right), \tag{15}$$

where $\vartheta \equiv tr\left(\mathbf{e}^{\mathrm{e}}\right)$ measures the elastic volume change, K_0, K_1, and μ are elastic stiffness coefficients and κ is a dimensionless, material-dependent scalar parameter that is assumed independent of strain rate and temperature. The deviatoric elastic strain tensor in the intermediate frame is defined by $\mathbf{e}^{\mathrm{e}'} \equiv \mathbf{e}^{\mathrm{e}} - \left(\vartheta/3\right)\mathbf{1}$. The function $z\left(\theta\right) = -\hat{c}\theta\ln\left(\theta/\theta_0\right)$ accounts for the purely thermal energy, with θ_0 a reference temperature at which $y = 0$. Thermoelastic properties are listed in Table 2.

The time rate of plastic deformation within each phase of the bulk material follows from

$$\dot{\gamma}^{(\alpha)} = \dot{\gamma}_0\left(\tilde{\tau}^{(\alpha)}/g^{(\alpha)}\right)^h \operatorname{sgn}\left(\tilde{\tau}^{(\alpha)}\right). \tag{16}$$

Above, $\dot{\gamma}_0$ and h are material parameters, $g^{(\alpha)}$ is the slip or shearing resistance, $\tilde{\tau}^{(\alpha)} \equiv j^e\tau^{(\alpha)}$, and $\operatorname{sgn}\left(x\right) = x/\left|x\right|$, with $\operatorname{sgn}\left(0\right) = 1$. Thermal softening at high temperatures is incorporated via

$$g^{(\alpha)} = g_0^{(\alpha)}\left(\theta/\theta_0\right)^r, \tag{17}$$

with $g_0^{(\alpha)}$ the flow resistance at reference temperature θ_0 and r a dimensionless constant. The following relationship is assumed between hardening and internal variable ξ:

$$\frac{1}{n}\sum_{\alpha=1}^{n}\left(g_0^{(\alpha)} - g_y^{(\alpha)}\right) = \hat{\alpha}\mu(\theta_0)\underbrace{b\sqrt{\rho_T}}_{\equiv\,\xi}, \tag{18}$$

with $g_y^{(\alpha)}$ an initial yield stress, b the magnitude of the Burgers vector in the reference lattice, and ρ_T the total dislocation line length per unit intermediate configuration volume associated with shearing impedance. The scalar proportionality factor $\hat{\alpha}$ accounts for dislocation interactions, while both lattice friction stress and effects of initial dislocation density are incorporated in the initial yield stress $g_y^{(\alpha)}$. Evolution of slip resistance at reference temperature θ_0 is dictated by a hardening-minus-dynamic-recovery relation:

$$\dot{g}_0^{(\alpha)} = A\sum_{\beta=1}^{n} q_\beta^\alpha\left|\dot{\gamma}^{(\beta)}\right| - Bg_0^{(\alpha)}\sum_{\beta=1}^{n}\left|\dot{\gamma}^{(\beta)}\right|, \tag{19}$$

where q is the latent hardening ratio in the interaction matrix

$$q_\beta^\alpha = \delta_\beta^\alpha + q(1-\delta_\beta^\alpha)\,. \tag{20}$$

Specifically for pure W grains, slip occurs in the $\langle 111 \rangle$ close-packed directions on any of the $\{110\}$ and $\{112\}$ families of planes, meaning the number of potentially active slip systems is $n = 24$. In the W-Ni-Fe binder phase, the number of potentially active slip systems is $n = 12$. Dislocations are assumed to glide in $\langle 110 \rangle$ close-packed directions on $\{111\}$ planes for this FCC metal. Parameters for the plasticity models are compiled in Table 3.

3.2 Interfacial fracture model

In the modeling framework exercised here, fractures may occur along W-W grain boundaries and W-matrix boundaries in the two-phase alloy. Intragranular cleavage and separation at matrix-matrix grain boundaries are not represented. Explanation and justification of the failure mechanisms and selected model parameters from experimental evidence can be found in earlier papers (Clayton, 2005a; b). More recently, Bless and Chau (2006) observed W grain-matrix separation in conjunction with cleavage fracture in this alloy. However, since the crack path is constrained to follow the inter-element boundaries in cohesive approaches of the present sort, intragranular fracture is not addressed in the current calculations. Mesh densities required to adequately address dependence of bulk (as opposed to interfacial) crack propagation and failure on arrangements of cohesive elements with deterministic, as opposed to statistically variable (cf. Zhou and Molinari, 2004), properties were anticipated to be computationally prohibitive upon consideration of the costly nonlinear constitutive updates of the deforming bulk material.

Fracture surfaces initiate at interfaces when the traction resolved on the potential initiation site exceeds the intrinsic strength of the interface. This strength is assumed to be a temperature-dependent material parameter. Fracture initiates following the local stress-based criteria

$$\hat{s} = \hat{s}_0 + \hat{s}_1(\theta - \theta_0), \qquad \hat{\tau} = \hat{\tau}_0 + \hat{\tau}_1(\theta - \theta_0), \tag{21}$$

where $\hat{s}$ and $\hat{\tau}$ are the resolved normal traction and shear traction on the interfacial surface, per unit reference area, and $\hat{s}_0$ and $\hat{\tau}_0$ are material parameters describing the normal and tangential (i.e., mode I and mode II) fracture strengths of the interface at reference temperature θ_0. Linearly temperature-dependent initiation strengths—capturing ductile-brittle transitions, for example—are captured by nonzero values of $\hat{s}_1$ and $\hat{\tau}_1$, and mixed-mode initiation criteria are specified by the ratio $\hat{s}_0 / \hat{\tau}_0$.

Degraded material at cohesive interfaces, subsequently following fracture initiation, supports local stresses decaying with separation distance as follows:

$$\begin{aligned} \hat{s} &= \left(\hat{s}_0 + \hat{s}_1(\theta - \theta_0)\right)\left(1 - \frac{\delta_n}{\delta_c}\right), && \text{(loading)} \\ \hat{s} &= \left(\hat{s}_0 + \hat{s}_1(\theta - \theta_0)\right)\left(1 - \frac{\delta_{n1}}{\delta_c}\right)\frac{\delta_n}{\delta_{n1}}, && \text{(unloading)} \end{aligned} \tag{22}$$

$$\hat{\tau} = \left(\hat{\tau}_0 + \hat{\tau}_1\left(\theta - \theta_0\right)\right)\left(1 - \frac{|\delta_t|}{\delta_c}\right)\left(1 - \frac{\langle \delta_n \rangle}{\delta_c}\right)\mathrm{sgn}\left(\delta_t\right), \qquad \text{(loading)}$$
$$\hat{\tau} = \left(\hat{\tau}_0 + \hat{\tau}_1\left(\theta - \theta_0\right)\right)\left(1 - \frac{|\delta_{t1}|}{\delta_c}\right)\left(1 - \frac{\langle \delta_n \rangle}{\delta_c}\right)\frac{\delta_t}{|\delta_{t1}|}, \qquad \text{(unloading)} \tag{23}$$

with δ_n and δ_t the normal and tangential crack openings, δ_{n1} and δ_{t1} the maximum values of δ_n and δ_t achieved over the deformation history, and δ_c a material parameter describing the separation distance beyond which the cohesive interface no longer supports loading. The Macaulay bracket is defined by the operation $2\langle x \rangle = x + |x|$. Prior to attainment of either of criteria (21), heat conduction proceeds as if the interface were perfectly bonded. Upon initiation of damage and subsequent separation, null heat flux conditions are enforced normal to the fracture surface. Interface properties used in the simulations are listed in Table 4.

3.3 Numerical simulations

Constitutive models presented for bulk and interfacial responses, respectively, were implemented within an explicit Lagrangian finite element solver (Clayton, 2005b; Johnson et al., 2001). The deformation gradient is integrated temporally via

$$\mathbf{f}_{t+\Delta t} = \exp\left(\mathbf{l}\Delta t\right)\mathbf{f}_t \ , \tag{24}$$

where $\mathbf{l} = \dot{\mathbf{f}}\mathbf{f}^{-1}$ is the velocity gradient that is assumed constant over the time interval $\left(t, t+\Delta t\right)$. The constitutive update proceeds in parallel at each integration point. Contributions to the energy balance (14) are calculated, and then the temperature field is updated explicitly (Johnson, 1981). Contributions from cohesive elements to global mechanical and thermal force vectors are then calculated prior to the enforcement of external boundary conditions and initiation of the integration step for the deformation field of the next cycle. The stable time increment is chosen as a small fraction of the time needed for a longitudinal elastic wave to traverse the smallest element in the mesh.

Two-dimensional calculations were conducted, with microstructures for meshing obtained from cross-sectional samples of a kinetic energy (KE) rod of the WHA material as shown in Fig. 2. Fields-of-view from three different microstructures were considered, as shown in Fig. 4, each a square window of size $L = 150\ \mu\mathrm{m}$. The microstructure exhibiting nearly equiaxed grains is labeled Transverse-1, whereas those with elongated grains are labeled Axial and Transverse-2, respectively. Note from the left image in Fig. 2 that the line-VISAR system is oriented perpendicular to the major axis of the ellipsoidal grains in microstructure Axial. Microstructure Transverse-2 was obtained by rotating the Axial microstructure 90° clockwise. Realistic lattice orientations depending upon spatial location were obtained from EBSD measurements performed on the samples and were used as initial conditions in the simulations. It is expected that there would be some variation in microstructures reconstructed from EBSD measurements of other regions of the sample of material, but a comprehensive treatment of such variation is not considered in the current work. Small gradients in initial lattice orientations within grains, evident in Fig. 2, were captured; i.e., grains were not initially homogeneous. The meshes of triangular elements conform to the microstructure and are selectively refined in the

vicinity of grain and phase boundaries to better resolve fracture surfaces.

In Fig. 4 and henceforth, in-plane spatial coordinates will be denoted by the conventional notation $x = x^1$ and $y = x^2$. Analyses were plane strain in the $x-y$ plane, representing columnar polycrystals extended infinitely in the out-of-plane direction. Out-of-plane elastic and plastic deformations were permitted so long as the total deformation field remained planar. The lower and upper edges of the domain are denoted by reference coordinates $Y = X^2 = 0$ and $Y = X^2 = L$, respectively. Left and right edges are denoted by $X = X^1 = 0$ and $X = X^1 = L$, respectively. Velocity initial and boundary conditions were prescribed as

$$\begin{aligned}
&\dot{x} = 0.5V_I\left(t/10^{-9}\text{s}\right) \quad \begin{cases} \text{for } 0 \le t \le 10^{-9}\text{s} \\ \text{along } X = 0 \end{cases} \\
&\dot{x} = \ 0.5V_I \begin{cases} \text{for } 10^{-9}\text{s} \le t \le 10^{-8}\text{s} \\ \text{along } X = 0 \end{cases} \\
&\dot{x} = 0.5V_I\left(\left[\left(1.1\times10^{-8}\text{s}\right) - t\right]/10^{-9}\text{s}\right) \quad \begin{cases} \text{for } 10^{-8}\text{s} \le t \le \left(1.1\times10^{-8}\text{s}\right) \\ \text{along } X = 0 \end{cases} \\
&\dot{x} = 0 \begin{cases} \text{for } t \ge \left(1.1\times10^{-8}\text{s}\right) \\ \text{along } X = 0. \end{cases}
\end{aligned} \tag{25}$$

Above, V_I is the impact velocity. The factor 0.5 arises since in the corresponding experiments, the particle velocity of the shocked material is half of the impact velocity due to symmetry between the impactor and target materials. Note, however, that velocity boundary conditions (25) are not completely analogous to those of the two-body plate impact experiment, as will be apparent later upon examination of the local stress fields and free surface velocities, for example. Conditions (25) result in a rightward-moving compressive pulse of approximate duration 9 ns. Additionally, boundaries along $Y = 0$ and $Y = L$ were free of shear stress but fixed in the $y-$direction, providing uniaxial strain conditions, i.e.:

$$\begin{matrix} t^x = \sigma^{xy} n_y = 0 \\ \dot{y} = 0 \end{matrix} \text{ along } \begin{cases} Y = 0 \\ Y = L. \end{cases} \tag{26}$$

Note that in plate impact experiment the macroscopic state of strain is uniaxial (i.e., no out-of-plane deformation), but local heterogeneities may induce out-of-plane deformations at the mesoscale. In the simulations, the right boundary was traction free, i.e. $\sigma^{ab} n_b = 0$ along $X = L$ for $t \ge 0$, mimicking the free surface at which the line-VISAR measurements are made. Null heat flux conditions were enforced along the external boundaries, with a uniform initial temperature $\theta_0 = 300$ K. Note that the present set of boundary conditions does satisfy periodicity in the y-direction, i.e. $y\left(Y = 0\right) = y(Y = L) = 0$. While less restrictive periodic boundary conditions could be applied, perhaps more representative of a small volume of material embedded within a homogeneous viscous medium representing the macroscopic plate impact

sample (Espinosa and Zavattieri, 2003b), these were not pursued in the present work. Instead, the boundary conditions used here are considered more straightforward to apply and interpret, representing a plate impact test conducted directly on a mesoscopic volume of material.

Results from five spall simulations are discussed in Section 5. These are labeled with Roman numerals in Table 4 to distinguish them from the corresponding experiments labeled by number in Table 1. Parameters used in each simulation, specifically orientation of microstructure (Fig. 4) and impact velocity of Eq. (25), are shown in Table 4. Note that orientations Axial and Transverse-1 correspond to 2-D projections of those grain orientations investigated in the experiments. Note also that numbers and numerals in Tables 1 and 4, respectively, differ in some cases with regards to microstructures and impact velocities for experiments 1-5 and simulations I-V. Some caution must be used when comparing results of 2-D simulations with 3-D experiments. For example, the in-plane microstructures used in experiments 3 and 4 (Transverse-1), and simulations III and IV (Transverse-2), differ visibly. However, microstructure effects on spall fracture could be considered similar among these experiments and simulations, since all present relatively large grain boundary areas per unit volume perpendicular to the *x*-direction. This is in contrast to experiments 1 and 2 (Axial) and simulations I, II, and V (Axial or Transverse-1), which present relatively less grain boundary area per unit volume oriented nearly perpendicular to the loading direction.

4 Experimental results

The output of the line-VISAR was recorded on a Hadland Imacon 792 streak camera (experiments WHA-1 and 2) or a Hamamatsu H7700 streak camera (experiments WHA-3, 4, and 5). An example streak record is shown in Fig. 5. The vertical axis corresponds to position across the sample, while the horizontal axis is time *t*. Analyses were conducted as detailed previously (Trott et al., 2001) to yield velocity measurements at each bright line of the streak as well as three others equally spaced between the bright lines. In some cases, small amounts of data from the edge of the streak were discarded due to decreased image contrast or excessive noise. The result was a large set of free surface velocities, $u_p = \dot{x}\big|_{X=L}$, parameterized by time and position *y* across the sample. Small time corrections were made in the results to account for impactor tilt. This correction was done based upon a few contours of constant velocity in the middle of the initial shock wave. A time shift that was linear with position was performed so that these contours could be associated with constant arrival times. The spatial resolution of the line-VISAR system as configured in these experiments was approximately 70 μm, meaning that the local free surface velocities were recorded in 70 μm-spaced intervals in the *y*-direction.

4.1 Spatially-resolved velocity measurements for experiment WHA-2

The results of one experiment, WHA-2, are examined here in detail and viewed in a variety of ways. Later, the results from all experiments will be analyzed and compared. The free surface velocity for test WHA-2 is plotted as a surface in *y*-*t* space in Fig. 6. While it is difficult to see features of the initial shock in this view, the initial flat top for the shocked state and the subsequent spall pullback signature are readily apparent. One can also clearly see variations in velocity along the *y*-direction.

By spatially averaging the measurements along the free edge at each time instant, an average particle velocity $\overline{u}_p$ can be found as

$$\overline{u}_p = \frac{1}{L}\int \dot{x}\big|_{x=L}\, dy\,, \tag{27}$$

as shown in Fig. 7. This average has been shown to have the same shock arrival and rise time as a conventional point VISAR measurement for sugar (Trott et al., 2006; Trott et al., 2001) and HMX (Trott et al., 2002), but significant variations between the two measurements were found after the shock arrival. Since it is difficult to correlate impact time to the VISAR measurement, the time of the records is adjusted so that the base of the average curve arrives at the measured ultrasonic sound speed of the material. Therefore, in Fig. 6 and subsequent plots, $t = 0$ corresponds to the instant of impact. From the average velocity history, it is possible to see the ramping elastic foot in front of the main shock wave consistent with the previous VISAR measurements on WHA (Bless and Chau, 2006; Dandekar and Weisgerber, 1999). The elastic ramp is followed by a plastic (bulk) wave that also has a finite rise time. The bulk wave is followed by a region over which the particle velocity is relatively constant. At about 1.2 μs after impact, the particle velocity decreases as unloading waves arrive from the back of the impactor. Eventually, the interaction of unloading waves leads to tensile failure of the sample (spall) which appears as the increase in particle velocity as the fractured material accelerates relative to the remainder of the sample. Spall will be discussed in detail in Section 4.3. The remainder of the velocity record consists of wave reverberations within the spalled material with a period of slightly less than 1 μs.

The variation in particle velocity is illustrated in two ways in Fig. 7. First, the range of data obtained is shown as the colored band above and below the average value. In general, the width of this band is nearly constant, though it is nearly invisible in the first shock. Second, the standard deviation of the velocities, $S(u_p(y,t))$, for a given time (scaled by a factor of 10 for clarity) is also shown in blue. The velocity distributions for each time are relatively normal in character, though for 20-40% of the data after the initial arrival of the wave, the null hypothesis can be rejected at the 95% confidence level based on the χ^2 test. For this experiment, the standard deviations are nearly invariant with respect to time except at the initial shock front. There, relatively small differences in the arrival time of the wave can result in fairly large deviations from the average. This behavior is quite similar to that seen in experiments on sugar (Trott et al., 2006) except the peak to plateau ratio is 4-5 for sugar and 2-2.5 in this experiment. The variations in particle velocity prior to arrival of the main shock provide an indication of the noise inherent in the line-VISAR. The baseline variation is 10-20% of the steady-state variation.

Temporal variations in the arrival of the initial shock wave can be seen more readily by viewing velocity contours in the y-t plane as shown in Fig. 8. The contours are clearly variable across the width of the specimen, with the variation being largest for low (0.05 km/s) and high (0.30 km/s) velocity contours. Variability at the low velocity is likely due to local differences in matrix concentration or crystallographic orientation of the grains. The variation at the higher velocity is only larger in the region of y = 0-1000 μm. For contours between these extremes, the spatial variation is comparable. In general, these variations have periods on the order of 1 mm, significantly larger than the sizes of individual grains. Thus, the variations are thought to be caused by variations in elastic and plastic properties of ensembles of grains for some depth below the free surface at which measurements are made.

By subtracting the spatially averaged velocity of Fig. 7 from the local velocities in Fig. 6, i.e.,

$$\delta u_p(y,t) = u_p(y,t) - \overline{u}_p(t), \tag{28}$$

we obtain the spatially-resolved velocity deviations (δu_p) shown in Fig. 9. Significant peaks and valleys exist, especially near the arrival of the first shock, but dominant spatial and temporal scales in the velocity deviations are absent, in contrast to those previously observed in shock-loaded boron carbide (B_4C) (Vogler et al., 2004).

4.2 Effect of impact velocity and sample orientation

Effects of impact velocity and sample orientation can be deduced from the spatially averaged free surface velocities shown in Fig. 10. As the impact velocity increases, the rise time for the main (bulk) shock wave decreases as expected, but the transversely oriented samples have longer rise times than axially oriented ones. The edges of the plateau velocity region are more rounded for the transverse samples, and, although not visible in this figure, the elastic foot is more spread out for the transverse samples. The pullback associated with spall is somewhat smaller for the transverse experiments, as is ringing in the spalled plate.

The standard deviations of velocity versus time for experiments 1-4 are compared in Fig. 11. As seen previously in Fig. 7 for WHA-2, a significant peak in the velocity dispersion occurs at the shock front. This peak is about 25 m/s for impacts at 350 m/s versus about 15 m/s for 250 m/s impacts, with somewhat higher peaks for the transverse samples. After the peak, a plateau in dispersion exists until about 1.2 μs, with the value of the plateau of the 250 m/s experiments about half that of the 350 m/s experiments. This time (1.2-1.3 μs) corresponds with the decrease in particle velocity associated with unloading (the pullback signature). The dispersion of the experiments with 250 m/s impact velocity then increases to about 10 m/s, while the dispersion levels in experiments of 350 m/s impact velocity remain constant or increase only slightly.

Contours of the velocity at the shock front are non-uniform for particular experiment WHA-2, as shown previously in Fig. 8. Non-uniform contours also occur for the remainder of experiments 1-4 as shown in Fig. 12. The contours shown are of constant free-surface velocities equal to half the impact velocity (i.e. 125 m/s and 175 m/s). The fluctuations in the contours decrease for the higher impact velocity (350 m/s), consistent with the decreasing rise times that occur for the spatially-averaged responses. In fact, the local variations in the front contribute significantly to the rise time for the averaged response. The fluctuations are also higher and the contours more jagged for transverse than for the axial experiments at the same impact velocity. Standard deviations, S_t, for the temporal positions of the contours are 6.0, 3.8, 10.1, and 5.9 ns for WHA-1 to WHA-4, respectively. For both sample orientations, the ratio of S_t for experiments at 350 and 250 m/s is approximately 0.6, suggesting a scaling that is invariant to orientation. Approximately the same ratio is found when comparing S_t for axial and transverse samples.

4.3 Hugoniot results

The macroscopic deformations of the WHA samples were determined from the average free-surface velocity histories using the Rankine-Hugoniot jump conditions for conservation of mass and momentum across a steady wave, though the steadiness of the waves has not been determined experimentally. Because the shock wave separates into elastic and plastic components, it must be analyzed in two steps as described, e.g., in Vogler et al. (2004). In all cases, impact was assumed to be symmetric so that the particle velocity of the shocked material

is half of the impact velocity. This assumption is acceptable since the macroscopic mechanical responses of the longitudinal impactors and transverse samples are roughly equivalent. The Cauchy stress ($\sigma = \sigma^{11}$) - volumetric strain ($\varepsilon = \rho_0/\rho - 1$) behavior for the current experiments, along with that from Dandekar and Weisgerber (1999), are shown in Fig. 13 and listed in Table 1. The current results agree with the earlier results except for experiment WHA-5, which is probably due to the aforementioned difficulties with that experiment affecting the accuracy of that measurement. For the other impact velocities, the macroscopic responses of the transverse samples were slightly more compliant than their longitudinally oriented counterparts, possibly a result of anisotropic work hardening during processing or grain elongation in the longitudinal direction. The HEL deduced from the average free surfaces velocities for the five current experiments varies widely. This is largely due to the spread out nature of the elastic wave and lack of a distinct break associated with yielding. Indeed, after consulting individual velocity records from a given experiment, a wide range of waveforms was observed. This variability may be due to fluctuations in phase composition or grain orientations among vicinities where local measurements were made. The average of the value of the HEL for all five experiments is 2.5 GPa, with most of the values close to that. This is in reasonably good agreement with the value of 2.76 GPa obtained previously for a similar material (Dandekar and Weisgerber, 1999).

4.4 Statistics of spall strength

Dynamic tensile failure in uniaxial strain loading, typically referred to as spall or spallation, frequently occurs in impact events, including the current plate impact experiments. A thorough discussion of spall phenomena can be found in Antoun et al. (2003). The spall strength of a similar variety of WHA to that currently studied has been measured to be 1.7-2.0 GPa (Dandekar and Weisgerber, 1999). In a typical spall experiment, impact sends a shock wave (or elastic and plastic waves, depending upon stress level) through both the target and impactor. Propagation of these and subsequent waves is shown schematically in Fig. 14, and the states of the material in the stress-particle velocity plane are shown in Fig. 15. The initial shocked state is labeled as **I** in this figure. When the compression waves reach the back of the target, a stress-free surface, and the back of the impactor, which has a low-impedance material against it, some or all of the wave reflects as an unloading wave. This unloading wave from the free surface at the back of the target, also referred to as a rarefaction fan because of its tendency to spread out as it propagates, unloads the sample to zero stress and the particle velocity shown as **II**. Note that this free surface velocity is somewhat lower than the impact velocity due to hysteresis associated with plastic deformation and other dissipative mechanisms. When the two rarefaction fans begin to intersect one another, they load the material into tension. If the rarefactions are of sufficient magnitude, the material will fail dynamically in tension (**III**) and unload to zero stress (**IV**). For the current experimental setup with a target to impactor thickness ratio of 2:1, tensile failure will occur in the vicinity of the midplane of the target as shown in Fig. 14. If the impedance of the material in tension is known, the spall strength can be determined from the so-called free-surface pullback velocity Δu (see Fig. 10). However, the instantaneous impedance is typically not known when the material deforms plastically. Dandekar and Weisgerber (1999) attempted to determine the impedance of WHA directly through concurrently backing the target material with void and PMMA. By assuming the same spall strength is reached in the two cases, the impedance can be found. However, we shall see that significant variations in the apparent spall strength for various positions render the validity of this assumption questionable. Instead, in the current investigation we calculated the slope (impedance) from the shocked state (**I**) to the

unloaded state (**II**) in the σ-u_p plane of Fig. 15 and assumed the same slope in the tensile regime.

The results for experiment WHA-2 are first examined in detail, and then differences between this test and the other experiments are considered. The average peak particle velocity u_1, the pullback velocity u_2, and their difference Δu_{fs} are shown versus position y in Fig. 16. Clearly, the pullback velocity varies considerably with position in the sample. Utilizing the unloading slope, U_t, as described above, the local spall strength can be calculated as

$$\sigma_{sp} = \rho_0 U_t \Delta u_{fs} / 2 . \tag{29}$$

The impedance $\rho_0 U_t$ assumed in the current for this experiment of 82 Gg/m^2 s is higher than the range 64-76 Gg/m^2 s found by Dandekar and Weisgerber (1999) but lower than the value of 92 Gg/m^2 s one would use if an elastic wave were assumed. The probability distribution of these spall strengths is shown in Fig. 17. The average value of spall strength for this experiment is $\bar{\sigma}_{sp}$ = 2.13 GPa, somewhat larger than the spall strength $\sigma_{sp}(\bar{u}_p)$ = 2.01 GPa inferred from the spatially averaged particle velocity. The averaging of particle velocities tends to smooth out local particle fluctuations so that u_2 is higher and u_1 is lower in the spatially averaged case. The standard deviation of the spall strengths for this experiment, $S(\sigma_{sp})$, is 0.37 GPa. Such a large value may explain why significant variations are sometimes seen in spall experiments on the same material (Baoping et al., 1994; Bless and Chau, 2006; Dandekar and Weisgerber, 1999). As it is customary to represent reliability and strength of mechanical parts with Weibull distributions (Weibull, 1951), a Weibull fit to the spall data, performed using the maximum likelihood method (Bury, 1975; Lu et al., 2002), is also shown in Fig. 17. We note, though, that there is no statistical support for choosing a Weibull distribution over a normal distribution for spall strengths in this experiment. The first Weibull parameter, σ_0, is close to the average, while the modulus, β, is 6.13. Weibull moduli of 5.5 for flexure and 6.9 for tension of sintered tungsten have been reported elsewhere (Margetson and Sherwood, 1979). Note that generally, the lower the Weibull modulus β, the greater the scatter in the data; as a rule of thumb, the Weibull modulus of a set of data is approximately equal to the mean of the data divided by its standard deviation.

Spall parameters for all experiments are given in Table 6. The average spall strengths $\bar{\sigma}_{sp}$ for transversely oriented samples (WHA-3 and WHA-4, grains elongated perpendicular to the loading axis) are generally 10-20% lower than for the axially oriented samples (WHA-1 and WHA-2, grains elongated parallel to the loading axis) at the same impact velocity. A possible explanation for this effect, upon consideration of the microstructure and numerical results, will be given later in Section 6. The standard deviation and Weibull modulus, though, are about the same at 0.33 GPa and 5-7, respectively, for all experiments except WHA-5, which exhibits more spatial variability. For reasons explained above for particular experiment WHA-2, the spall strength from the average particle velocity, $\sigma_{sp}(\bar{u}_p)$, is always lower than the average spall strength $\bar{\sigma}_{sp}$.

5. Numerical results

Recall that boundary conditions listed in Eq. (25) result in a compressive stress wave moving from left to right in the microstructure, i.e., the positive *X*-direction. This wave reflects off of the free surface at $X = L$ at around $t = 37$ ns, producing a release wave and leading to initiation of spall at around $t = 40$ ns. Contour plots of Cauchy pressure p (mean stress), elastic energy density ψ^e, cumulative plastic strain ε^p, and dislocation density ρ_T are shown in Figs. 18 and 19 for simulations WHA-III and WHA-IV, respectively. These variables are defined by

$$p = -tr(\boldsymbol{\sigma})/3\,, \tag{30}$$

$$\psi^e = K_0(\theta)\vartheta^2/2 - K_1\vartheta^3/3 + \mu(\theta)\mathbf{e}^{e\prime} : \mathbf{e}^{e\prime}\,, \tag{31}$$

$$\varepsilon^p = \int \sqrt{(2/3)\mathbf{d}^p : \mathbf{d}^p}\, dt\,, \qquad \mathbf{d}^p = sym\left(\mathbf{l}^p\right), \tag{32}$$

$$\rho_T = \left[(\hat{\alpha}\mu(\theta_0)bn)^{-1} \sum_{\alpha=1}^{n} \left(g_0^{(\alpha)} - g_y^{(\alpha)} \right) \right]^2 . \tag{33}$$

The same color scales are used in Figs. 18 and 19 to facilitate comparison. Note that regions of large tensile pressures develop near the impending spall plane, towards the right quarter of each sample. Correspondingly, large elastic energies occur in the same regions. Plastic strains tend to be largest in the more ductile matrix phase, which also undergoes more strain hardening and dislocation accumulation. Comparing Fig. 18 (WHA-III, impact velocity 250 m/s) with Fig. 19 (WHA-IV, impact velocity 350 m/s), local pressures, energies, plastic strains, and dislocation densities all generally increase with increasing magnitude of the impact velocity. Note also that over the time duration of the simulations, local plastic strain rates on the order of $\dot{\varepsilon}^p = 10^7$ s^{-1} were attained (i.e., plastic strains in excess of 0.1 were achieved over time periods on the order of ~10 ns).

Contours of effective stress σ^{eff} are shown for all simulations, after spall has occurred, at $t = 60$ ns in Fig. 20 and $t = 80$ ns in Fig. 21. The effective stress in Figs. 20 and 21 is defined as

$$\sigma^{eff} = \sqrt{(3/2)\boldsymbol{\sigma}' : \boldsymbol{\sigma}'}\,. \tag{34}$$

Notice that effective stresses relax as a result of fracture, as indicated by slightly lower stress values, in general in the microstructures of Fig. 21 relative to the same microstructures in Fig. 20. However, comparing results for the same microstructures conducted at different impact velocities, spall fracture tends to be more chaotic with increasing velocity, with larger local element distortion and generally larger crack opening displacements. For example, fracture is more severe in simulation WHA-V (450 m/s) than WHA-II (350 m/s), and is more severe in WHA IV (350 m/s) compared to WHA-III (250 m/s). Note that fracture occurs most readily for simulations of the Transverse-2 microstructure, WHA-III and WHA-IV, with apparently the largest number of available grain boundary facets per unit area oriented nearly perpendicular to the wave propagation direction. Also notice that the spall fracture planes do not cut cleanly across the material, but rather ligaments of highly stretched material hold the sample together where insufficient grain boundary facets (i.e., cohesive finite elements in the numerical context) exist to propagate cracks across the domain. Presumably in an actual material, cleavage fracture (absent in the present model) would facilitate complete spall fracture of the sample.

Two quantitative indicators of the degree of damage induced in the sample by micro-cracking are specified as follows:

$$\Gamma = \sum_j \left(l\sqrt{\delta_n^2 + \delta_t^2} \right)^{(j)}, \qquad \Omega = A^{-1} \sum_k (l)^{(k)}, \tag{35}$$

where summation in the first of (35) is invoked over j micro-crack segments of length l, with crack opening displacement $\delta = \sqrt{\delta_n^2 + \delta_t^2}$. In the second of (35), summation is invoked over k micro-cracks satisfying the fully opened criteria $\delta \geq \delta_c$, and $A = L^2$ is the area of the domain. For purely normal separation, Γ of (35) is the 2-D analog of the total volume of free or void space in the sample produced during spall, and Ω of (35) is the scalar crack density (i.e., crack length per unit area). As indicated by the value of Γ in Fig. 22(a), significant damage evolution commences around t = 40 ns in all simulations. Damage accumulates at the slowest rates in simulations I and II, as can be deduced from visual inspection of Figs. 20 and 21. The largest crack opening displacements occur in simulations IV (elongated grains oriented perpendicular to loading at intermediate velocity of 350 m/s) and V (equiaxed grains with highest impact velocity of 450 m/s). As shown in Fig. 22(b), numerous cracks do not reach a fully opened state, $\delta \geq \delta_c$, in the simulations until around t = 50 ns. As shown here, the largest crack densities accumulate in simulations of microstructure Transverse-2, cases WHA-III and WHA-IV. Some crack closure occurs in simulation WHA-II, for example, as evidenced by fluctuations (in particular, small local reductions) in Ω with increasing simulation time.

As was done for the experiments, free surface velocity statistics are first investigated here in detail for one simulation (WHA-IV), then in general for all simulations. The free surface velocity history, $u_p(y,t)$ for WHA-IV is shown in Fig. 23. Note that the peak local free surface velocity only reaches 311 m/s at t = 36 ns, even though the 'impact velocity' V_I of Eq. (25) was 350 m/s. This phenomenon is attributed to two causes: attenuation of the initial loading wave by the fixed boundary condition in (25) for t > 10 ns, and energy dissipation from inelastic deformation during wave propagation. If the impact velocity were held fixed at 350 m/s over the full duration of the simulation, eventually the free surface would attain a rigid-body velocity of 350 m/s, once wave refections subside. Spatial fluctuations in u_p with spacing on the order of the grain size, 10-30 μm, or even smaller, are apparent in Fig. 23 and in the plot of the velocity perturbation $\delta u_p(y,t)$ in Fig. 24. Significant fluctuations initiate at around 37 ns, when the maximum velocity is achieved at the free surface, and reach their largest magnitude around 45 ns (post spall). Contours of free surface velocity in the y-t plane are shown in Fig. 25, analogous to the plot of experimental data in Fig. 8. Heterogeneities in the wave shapes on the order of the grain size are apparent in the initial elastic wave (50 m/s) and for low velocity contours (100 m/s - 200 m/s). Heterogeneity increases drastically as a result of heterogeneous plastic deformation at later times, i.e. for t >34 ns.

Spatially averaged free surface velocity histories, $\overline{u}_p$, are shown in Fig. 26. Generally, the higher the impact velocity, the higher the peak velocity or maximum value of $\overline{u}_p$ over the duration of the simulation, as expected. Differences between average particle velocity curves corresponding to the same impact velocity are due to differences induced by the microstructure. For example, localization and heterogeneous plastic strain lead to different peak velocities among simulations II and IV, while final velocities at t = 80 ns differ due to different spall

behavior. Note that nonzero free surface velocities at late times are a result of the motion of the ejected, separated, or spalled material. Standard deviations, $S(u_p)$ in free surface velocity are depicted in Fig. 27. For a given microstructure, the higher the impact velocity, the greater the dispersion or variance in particle velocity. For example, compare WHA-III (generally lower *S*, impact velocity of 250 m/s) with WHA-IV (higher *S*, 350 m/s), or WHA-II (lower *S*, 350 m/s) with WHA-V (higher *S*, 450 m/s). This result is expected considering the character of the spall planes shown in Figs. 20 and 21. At a fixed velocity of 350 m/s, simulations with of microstructure Transverse-1 (WHA-II) tended to exhibit the smallest $S(u_p)$, perhaps because its nearly equiaxed grains produced the least spatial variation in response. Shown in Fig. 28 are contours of constant free surface velocities for all simulations, analogous to the experimental data in Fig. 12. Here, traces of constant velocity $V_I/2$ are shown: 125 m/s for WHA-III, 175 m/s for WHA-I, II, and IV, and 225 m/s for WHA-V. Note that simulations WHA-II and V display the most uniform wave shape (both with equiaxed microstructure Transverse-1), with a few fluctuations on the order of the grain diameter for $y > 80$ nm. Simulations WHA-III and IV (microstructure Transverse-2) display some variations on the order of the grain diameter, as well as some smaller fluctuations. Finally, simulation WHA-I shows grain-scale fluctuations in the interior of the sample, $30 < y < 120\ \mu\text{m}$, with significant attenuation of the wave near the lateral boundaries at $y = 0$ and $y = L$. For this particular simulation (WHA-I), significant local heating and plastic strain localization caused a drop in the material's stiffness along the lateral boundaries, and a corresponding reduction in local plastic wave velocity.

Shown in Figs. 29 and 30 are contours of particle velocity magnitude $|\mathbf{u}_\mathbf{p}|$ and effective stress σ^{eff} for simulations WHA-I (Fig. 29) and WHA-IV (Fig. 30), at *t* = 20 ns, when the impact wave has traversed roughly 2/3 of the sample. Particle velocity vectors are also shown, superimposed on the contours of $|\mathbf{u}_\mathbf{p}|$ and scaled by magnitude. Vortices in material motion, with characteristic lengths on the order of the grain size, are apparent in the wake of the elastic-plastic stress wave. These vortices do not appear to occur preferentially within particular grains or a particular phase of the alloy, however. Heterogeneities in the wave front induced by the microstructure are also obvious. Comparing Fig. 29(a) with 30(a), the reduction in particle velocity near the lateral edges $y = 0$ and $y = L$ is apparent in the former (WHA-I). From the stress contours, W grains tend to support relatively larger effective stresses than the more ductile binder phase. Comparing Figs. 18 and 19 with 29 and 30, note that momentum conservation requires that the pressure be more uniform than the effective deviatoric stress; i.e., for the boundary conditions applied here, W grains tend to support larger effective stresses than the binder, but pressures are not preferentially higher in either phase.

Spall statistics for the simulations are shown in Table 7. Because the wave mechanics for the problem domain and boundary conditions of Eq. (25) do not correspond to those of a macroscopic plate impact test, the free surface velocity profiles differ (compare Figs. 10 and 26, for example), and Eq. (29) does not apply for the simulations. Instead, the following simple relation was formulated specifically for computing spall strength when the boundary conditions (25) are used:

$$\sigma_{spall} = \hat{I}\left(u_p^{\max} - u_p^{\min}\right), \quad \forall u_p^{\min} > 0, \tag{36}$$

where $u_p^{\max}$ is the peak particle velocity, $u_p^{\min}$ is the minimum velocity over the post-peak time interval $40 \text{ ns} \le t \le 80 \text{ ns}$, and $\hat{I}$ is an effective impedance chosen such that the average spall strength from simulation WHA-I was 2.0 GPa, matching the cohesive tensile strength of Table 4, and in agreement with the spall experiment (e.g., #311-2 with point VISAR) on WHA of Dandekar and Weisgerber (1999). Although not rigorous, (36) is intuitively correct in that the higher the value of $u_p^{\min}$, the greater the residual velocity of the spalled material, and hence the lower the spall strength. Likewise, the larger the value of $u_p^{\max}$, the greater the force of the tensile release wave resisted by the material. Although inexact, (36) has value in that it can be used to judge trends in the data for comparison with the physical spall experiments. Note that when $u_p^{\min} = 0$, Eq. (36) does not apply, as $\sigma_{sp} \to \infty$. Parameters for probability distributions, both Gaussian and two-parameter Weibull, were computed as was done for the experiments. Just as in the experiments, in all simulations the spall strengths computed from the average velocity, $\sigma_{sp}(\bar{u}_p)$, are lower than the average spall strengths $\bar{\sigma}_{sp}$, as differences among local maxima and minima in free surface velocities over the time history are smoothed out by averaging in the former. Simulations WHA-III and WHA-IV exhibit the lowest relative spall strengths, which can be further explained by Figs. 20 and 21: relatively more continuously linked fracture sites are available for this microstructure with grains elongated perpendicular to the loading/unloading direction of wave propagation. The most spall-resistant microstructure at the moderate impact velocity (V_I =350 m/s) is Transverse-1 (WHA-II, $\bar{\sigma}_{sp} = 2.88$ GPa), while Transverse-2 is the least resistant to spall fracture (WHA-IV, $\bar{\sigma}_{sp} = 1.50$ GPa), for the reason noted above. Standard deviations $S(\sigma_{sp})$ range from 0.1 - 0.2 GPa, except for simulation WHA-I. This case exhibits the largest variation in spall ($S(\sigma_{sp}) = 0.31$), which agrees with the velocity scatter evident in Fig. 27 for that simulation. Computed Weibull moduli range from 7.82 to 18.77.

6 Discussion

One objective of the present work is assessment of the feasibility of comparison of results from spatially resolved plate impact tests with microstructure scale plasticity and fracture simulations. Such comparisons permit one to understand phenomena in a way not available through experiments or modeling alone and suggest means of potential improvement in the existing techniques.

Regarding free surface velocity profiles:

- Spatial fluctuations on the order of several or tens of grains (~0.5 mm) are observed in free surface velocity profiles collected from the experiments (Figs. 8, 9, and 12).
- Spatial fluctuations on the order of the grain size (~10-30 microns) are apparent in many of the free surface velocity profiles collected from the simulations (Figs. 23-25 and 28).
- Standard deviations in spatially resolved free surface velocity, $S(u_p)$ are typically on the order of 10 m/s for experiments (Fig. 11), and 10-30 m/s for simulations (Fig. 27).
- A significant spike is seen in the standard deviation of the free surface velocity at the time of arrival of the initial shock in the experiments, but no such spike is evident in the simulations.
- Following the initial spike, the standard deviation remains relatively constant in the

experiments, though most show a moderate change when the particle velocity increases (the pullback signature). Some simulations show a similar behavior, but others decrease or increase noticeably, though the time scale of the simulations is significantly shorter in the simulations than in the experiments.

Regarding spall fracture,

- The experimental results indicate that the transverse orientation exhibits the lowest spall strength, as reported in Table 6. The magnitudes of differences in spall strengths for samples with different microstructures were inconsistent, however. The difference in average strengths $\bar{\sigma}_{sp}$ between WHA-1 and WHA-3 is 0.07 GPa (both tests at 250 m/s impact velocity), whereas the difference is 0.46 GPa between WHA-2 and WHA-4 (both at 350 m/s). Similar trends apply for the Weibull parameter σ_0.
- The computations indicate that the Transverse-2 microstructure exhibits the lowest spall strength, as reported in Table 7.
- Experimentally, higher velocity impacts yield a somewhat higher spall strength, $\bar{\sigma}_{sp}$, for both orientations. In contrast, the simulations have somewhat lower spall strength when the impact velocity is increased.
- In experiments and modeling, no relationships between microstructure, impact velocity, and standard deviations of spall strength are apparent (Tables 6 and 7). Values of $S(\sigma_{sp})$ tend to be slightly smaller among simulations (most less than 0.2) than among experiments (most ranging from 0.3 to 0.4).
- Values of Weibull modulus β are significantly higher among simulations (Table 7, ranging from 7.8 to 18.8) than experiments (Table 6, ranging from 3.5 to 6.9).
- Comparison of the statistics $S(\sigma_{sp})$ and β demonstrates that even though average spall strengths roughly agree between experimental and model results, the shapes of the distributions do not.

Differences in free surface velocity profiles arise naturally as a result of differing scales of resolution in the experiments and models. From the above observations, the simulations reflect local heterogeneity of wave propagation induced by the differences in deformations among individual grains and the softer matrix phase surrounding them, whereas the experiments detect gradients in microstructure properties among aggregates of grains, reflected in the free surface velocity data.

The spatial resolution of the experiments is established by the capabilities of the line-VISAR instrument. The resolution along the line can be varied, but optical instrumentation limits its minimum to around 15-20 microns. However, even if the nominal resolution is 15 microns, each measurement encompasses the response of about 60 microns of material because of the procedure used for data collection and analysis. Decreasing the resolution along the line also results in a reduction in the amount of material that is being monitored by the instrument. Depending upon the dominant length scales for material behavior, monitoring a smaller amount of material may cause important behaviors to be missed. It may also affect the reliability of statistics associated with material failure.

The spatial resolution of the simulations is established by the finite element discretization. The approach here has been to use the finest FE mesh permissible within

computing constraints. These elements used here are of small enough size, with typical elements on the order of 1 μm in dimension in the vicinity of grain boundaries, to resolve critical cohesive zone lengths and compute, with precision, the average material response (e.g., homogenized stress-strain behavior) as discussed in (Clayton, 2005a; b). However, minute aspects of fracture and the local material response are inevitably sensitive to mesh construction and the corresponding degree of resolution of microstructure features. For example, the finer the mesh, the greater the potential for a more faithful representation of the actual microstructure in the numerical reconstruction, including initial lattice orientation gradients within grains and facets of potential fracture along grain and phase boundaries. More refined grids than those used presently were prohibitively expensive from a computational standpoint, but they would enable the possibility of detection of even smaller fluctuations in free surface velocities. Such finer grids were deemed unnecessary, since the elements used at present were small enough to detect features an order of magnitude smaller than the size of individual grains, and the grain size appeared to be the dominant feature or characteristic length reflected in the results of the simulations. To this end, averages and standard deviations of spall strength were also computed using only every other free surface node at $X = L$, and variations in these values were negligible with those presented in Table 7, computed using all free surface nodes. Furthermore, the element sizes used here are of comparable or smaller magnitudes than those used by others in similar investigations: Zhou et al. (1994) used a uniform grid of crossed triangles of size 1 μm in a study of oblique impact of WHA microstructures; Becker (2004) used a uniform grid of brick elements of size 3 μm in a study of shock wave propagation in polycrystalline tantalum; and Love and Batra (2005) used quadrilateral elements of size 5 μm to determine the elastic-plastic response and effective properties of tungsten particulate composites.

Substantial variability among the results from simulations is expected among different reconstructions of the material (i.e., microstructures reproduced from different regions of the material) of the present dimensions, on the order of fifty W grains. Variability is also present in physical experiments, even properties averaged over macroscopic dimensions. For example, differences in spall strengths exist among realizations in the present work and among the results of (Dandekar and Weisgerber, 1999). Thus, a statistically valid number of measurements of the spall strength must be made to fully capture the behavior. For conventional spall experiments, this entails a large number of experiments. When the line-VISAR is used, though, even a single experiment can provide a statistically valid number of measurements, provided the relationship between the line-VISAR measurements and material failure is understood. Reliance on a single experiment would also require that variations in material strength are consistent from sample to sample, something that has not yet been verified for this or any other material. Collection of definitive statistics on variability among samples of material with similar, but not identical, microstructures (e.g., samples of material of the same global orientation cut from different locations in the KE rod) would presumably require many more experiments and simulations.

Another source of discrepancy between simulations and experiments is differences in boundary conditions. Computational costs prohibit simulation of a two-body contact and impact problem with the present level of detail of resolution of both microstructure features and constitutive behavior for the impactor. The present approach, specifically Eq. (25), enables spall to take place in the simulations, and the results enable one to correlate trends in the response with features of the microstructure. However, the use of boundary conditions not identical to those used in the macroscopic experiments complicates comparison of results, particularly the wave shapes (e.g., fundamental differences exist between Figs. 10 and 26), and necessitates the use of

an approximate way to compute spall strength from the free surface velocity profiles obtained from the simulations (Eq. (36)).

Material properties used in the simulations have been discussed in detail elsewhere (Clayton, 2005a; b). However, it is worth noting that the parameters entering the plasticity theory (Table 3) were obtained via calibration to material strength data in both the quasi-static regime and dynamic regime of strain rates up to 3000/s (i.e., Hopkinson or Kolsky bar data). In the present simulations, local effective plastic strain rates reach magnitudes on the order of 10^7/s. Presently, experimental techniques providing homogeneous stress states at such high rates are unavailable for calibrating the plasticity model parameters of the materials of interest here. For example, small-scale Hopkinson bars can provide stress-strain data in the rate regime of up to $\sim 10^4$/s. There is even uncertainty as to whether the generally accepted forms of the kinetic equations for viscoplasticity (e.g., Eqs. (16)-(20)) are valid at such high deformation rates. Nonetheless, we elected to proceed with the simulations using the readily available dynamic properties, following the discussion of (Becker, 2004).

Finally, a discrepancy between experiments and simulations exists due to the 2-D nature of the simulations. Real materials have complex modes of deformation and failure, particularly with regards to evolution of fracture surfaces that cannot be faithfully captured by 2-D simulations. Future increases in computing power will make comparably detailed numerical studies of plasticity and fracture at the grain level feasible in three dimensions.

Mescheryakov and coworkers (Mescheryakov, 2003; Mescheryakov et al., 2004) developed a multiscale descriptive framework for describing effects of micro- or meso-structures on wave propagation in solids under impact loading. In their framework, dispersions of particle velocities are analyzed at three scales of increasing characteristic length: mesolevel-1, mesolevel-2, and macroscale. Instability under shock compression is characterized by exhaustion of dissipative mechanisms and attainment of a maximum value of dispersion at the finest length scale, mesolevel-1. Subsequently, dispersion at meso-level 2 increases as regions of localized shear or damage interact at a larger length scale, culminating in final failure or percolation of the sample (e.g., macroscopic spall failure). In this framework, the simulations indicate dispersion at the grain scale, corresponding to Mescheryakov's mesolevel-1, while the experiments are indicative of dispersion at a larger length scale not measurable in the simulations, mesolevel-2.

Case and Horie (2006) recently used a DEM to model impact and shock wave propagation in polycrystalline copper at the mesostructure level, with a level of resolution comparable to that used in the present work, though these authors did not attempt to model spall fracture explicitly. They also found that the particle velocity dispersion (i.e, standard deviation $S(u_p)$) at the shock front depends upon the impact stress, in agreement with the trends from the current experiments and simulations. They also found that eleven grains was insufficient to produce a steady impact wave (i.e., statistically constant shock front), in agreement with Figs. 29 and 30 of the present computational study. Also, in another DEM study of copper, Yano and Horie (1999) noted vortices in material flow in the wake of the shock pulse, similar in scale and appearance to those presented here in Figs. 29 and 30. In their work, non-uniform tensile stresses were observed where waves interact, indicating that a spall strength distribution can be obtained even with constant material strength. Such is also the case in the present study, where a distribution of spall strengths was found for a heterogeneous crystalline material with uniform cohesive strength. Finally, Case and Horie (2006) noted peaks in the particle velocity dispersion of about twice the magnitude of that found at later, stead-state times in the impact events. Such a

spikes were observed in the experiments, as shown in Fig. 11, but were absent in our numerical results, Fig. 25. According to Mescheryakov and Astroshenko (1992), such a peak should occur at the midway point of the plastic wave rise, when effects of mesoscopic rotations of material manifest most strongly. The reason for the absence of such a peak in the numerical results is not obvious at present. One possibility is that the kinetic equations for plasticity, with strain-rate hardening in (16)-(20), cause some smoothing of the plastic wave, as different plasticity kinetics were used in the study of Case and Horie (2006).

As remarked above, the transverse microstructure exhibits the lowest average spall strength in the experiments. Note that this microstructure presents a relatively large area per unit volume of grain boundary surfaces perpendicular to the loading direction, in contrast to the axial orientation, whose grains are elongated along the axis of impact (Fig. 2). Since the weakest link is expected to control failure, the transverse orientation should have average spall strengths that are lower than the axial orientation. For example, failure of a typically larger grain boundary facet elongated perpendicular to the loading direction would present a larger starter crack for eventual catastrophic fracture than would failure of a typically smaller grain boundary facet in a microstructure with equiaxed or shortened grains aligned perpendicular to the loading direction. In the simulations, the Transverse-2 microstructure possesses the lowest strength. The reason for this is clear from grain and phase boundary arrangements and examining the fracture sites in the simulations of Figs. 20 and 21. Since the primary fracture criterion in the simulations follows from the maximum resolved normal stress acting on grain or phase boundaries (Eqs. (21) and (22) and $\hat{s}_0$ of Table 4), those microstructures presenting the greatest number of contiguous fracture sites oriented perpendicular to the impact direction tend to fail most readily. For example, $\bar{\sigma}_{sp} = 2.00\,\text{GPa}$ for WHA-I (Axial microstructure, 350 m/s), while $\bar{\sigma}_{sp} = 1.50\,\text{GPa}$ for WHA-IV (Transverse-2 microstructure, 350 m/s). Note that simulations II and V, with the Transverse-1 microstructure, exhibit the highest average spall strength. Analogous trends arise for the Weibull parameter σ_0. Transversely oriented samples include both Transverse-1 and Transverse-2 orientations, depending upon how one views the sample. In the simulations, these microstructures are not equivalent, however. Even though both may have comparable grain boundary area per unit volume, microstructure Transverse-2 exhibits more grain boundary facets oriented most nearly parallel to the loading axis, and its lower spall strength reflects this characteristic.

The experiments indicate that higher velocity impacts produce a higher spall strength, $\bar{\sigma}_{sp}$. This suggests that the regions where failure occurs (e.g., W-matrix interfaces and W-W grain boundaries) are preconditioned to a more durable state by the initial compressive pulse. Such behavior has been observed previously in other brittle materials (Dandekar, 2004). Physically, this phenomenon could correspond to closure of microvoids or elimination of deleterious effects of other defects caused by impurities at the boundaries. On the other hand, the simulations predict somewhat lower spall strength when the impact velocity is increased, despite the increase in fracture toughness with temperature provided by Eq. (21). The correct behavior could be reflected in future simulations by incorporating cohesive traction laws dependent upon the stress history of the local material.

It is suggested here that initiation of spall fracture may be controlled by grain and phase boundaries, in agreement with experimental observations of (Weerasooriya, 2003). However, crack propagation and macroscopic spall behavior are thought to also require substantial grain cleavage: once a sufficiently large, a micro-crack initiated along grain/phase boundaries will then

propagate fully across the specimen, irrespective of the underlying microstructure. Post mortem inspection of fully fractured (i.e., spalled) specimens would then likely indicate both intergranular and cleavage mechanisms (Bless and Chau, 2006). The simulations (Figs. 21 and 22) also demonstrate that for complete fracture to occur, cleavage must take place, since insufficient fracture sites for purely intergranular fracture likely exist to allow for crack propagation across a sample of dimensions of several hundred μm or larger. This assertion was also made in (Clayton, 2005a) in the context of tensile loading. Grain and phase boundaries should also exhibit a distribution of strengths; for example, Weerasooriya et al. (1994) suggested that W-W boundaries are intrinsically weaker than W-matrix boundaries. Clayton (2005a) investigated the effect of variable ratios of grain and phase boundary strengths on uniaxial tensile failure. The role of such variable grain boundary strengths on spall fracture statistics remains to be investigated in future modeling work. Based on the current results, it is apparent that the variability in spall statistics observed experimentally is due both to the variable strengths and flaw distributions and to the multiphase polycrystalline microstructure of the material.

In the future, multiple realizations of the same experiments (i.e., same impact velocity and sample orientation) should be conducted to quantify sample-to-sample variability in wave propagation and spall properties. Analogously, additional simulations should be performed with microstructures of similar global characteristics (e.g., equiaxed vs. extruded grains) but different local characteristics (e.g., individual grain shapes and orientations). Such simulations would provide additional support for the hypothesized dependence of spall strength on orientation, for example.

7 Conclusions

A combined experimental-computational study, accounting for the effects of microstructure on wave propagation and spall fracture, was conducted on a tungsten heavy alloy subjected to normal plate impact loading. In the experiments, a line-VISAR system enabled the resolution of particle velocity profiles at the scale of tens of microns. In the simulations, crystal plasticity theory coupled with a cohesive zone model for intergranular and interphase fracture enabled the resolution of local thermo-mechanical response of the material at the micron scale.

The large volume of experimental data collected, and corresponding analysis of this data, provide a detailed description of the material's high rate behavior and mechanical properties. Specifically, for WHA microstructures of different microstructure orientations, the following information was obtained: spatially resolved free surface velocity profiles, Hugoniot elastic limits, spall strengths, and spall statistics. While the bulk HEL values and average spall strengths obtained here are comparable with results obtained from previous point-VISAR experiments (Dandekar and Weisgerber, 1999), the detailed statistical aspects of wave propagation and fracture have heretofore been unavailable. Such statistics may support future macroscopic modeling of dynamic deformation and failure of the WHA material. For example, the Weibull modulus may be used to provide initial conditions for simulations employing spatially variable failure properties (Brannon et al., 2007; Goto et al., 2007; Schraml et al., 2005; Zhou and Molinari, 2004).

From the simulations, local behavior not accessible in the experiments was observed. Plastic strain accumulation and dislocation activity tended to be greatest in the more ductile matrix phase of the WHA material, whereas larger effective deviatoric stresses were supported by the W grains. Heterogeneous impact wave propagation and vortices in material motion behind the plastic wave were found, at the scale of individual grains. Local fracture

morphologies were also observed, with details of micro-cracking dependent upon initial microstructure and impact velocity. Effects of microstructure orientation and impact velocity on statistics of spall fracture described here have not, to our knowledge, been quantified in previous modeling studies of WHA. In the simulations, these spall statistics arise strictly as a result of the dual phase granular microstructure, since a uniform value is used for the strength of the cohesive zone elements. One likely reason that the statistics in the simulations differ from those observed in the experiments is that the local fluctuations associated with spall strength in the experiments may be attributed to microstructural heterogeneities and to the presence of variable strength or flaw distributions.

In both experiments and simulations, similar effects of microstructure on average spall strengths were observed. Grain boundaries seemed to dominate fracture initiation in either case, with microstructures presenting the most area per unit volume perpendicular to loading direction exhibiting the least strength. Differing scales of resolution between model (fine resolution, but limited to small sample sizes) and experiment (larger sample, but less refined resolution) inhibited direct comparison of results. For example, variations in free surface velocity profiles on the order of grain size were observed in the simulations, while variations on the order of multiple grains were observed in the experiments.

The present study has suggested methods for improved concurrent experimental and modeling efforts in the future. In the experiments, a still unresolved issue is the effect of sample thickness on heterogeneous wave propagation. For example, the post-spall wave profiles include not only the effects of the heterogeneous fracture pattern, but also the effects of wave propagation through undamaged but heterogeneous material between the spall plane and the free surface. More refined techniques enabling in-situ study of the wave propagation and spall behavior on the scale of individual grains or even smaller (e.g. micron scale) would also be instructive. The present simulations permit correlation of local fracture behavior and microstructure effects to the simulated free surface velocity profiles. Incorporation of grain cleavage models for this particular alloy, and improvements in computational methods for dynamic crystal plasticity and cohesive fracture to address much larger sample sizes, with dimensions on the order of millimeters and at time scales on the order of microseconds, would enable more useful, direct comparison with plate impact experiments of the same dimensions.

Acknowledgements

The authors would like to thank Wayne Trott, Jaime Castañeda, and the STAR team for performing the line-VISAR experiments. Work at Sandia was supported through the Joint DoD/DOE Munitions Technology Development Program. Sandia is a multiprogram laboratory operated by Sandia Corporation, a Lockheed Martin Company, for the United States Department of Energy's National Nuclear Security Administration under contract DE-AC04-94AL85000. J.D.C. acknowledges support from the U.S. Army Research Laboratory (ARL). Todd Bjerke and William Edmanson (both of ARL) are thanked for obtaining the material specimens.

References

Antoun, T.H., Seaman, L., Curran, D.R., Kanel, G.I., Razorenov, S.V., Utkin, A.V., 2003. Spall Fracture. Springer-Verlag, New York

Argon, A.S., Maloof, S.R., 1966. Plastic deformation of tungsten crystals at low temperatures. Acta Metallurgica 14, 1449-1462.

Asaro, R.J., 1983. Crystal plasticity. Journal of Applied Mechanics 50, 921-934.

Asay, J.R., Barker, L.M., 1974. Interferometric measurement of shock-induced internal particle velocity and spatial variations of particle velocity. Journal of Applied Physics 45, 2540-2546.

Asay, J.R., Chhabildas, L.C., 2003. Paradigms and challenges in shock wave research. In: Horie, Y., Davison, L., Thadhani, N.N. (Eds.), High-Pressure Shock Compression of Solids VI: Old Paradigms and New Challenges. Springer-Verlag, New York, pp. 57-119.

Baer, M.R., Trott, W.M., 2004. Mesoscale studies of shock loaded tin sphere lattices. In: Furnish, M.D., Gupta, Y.M., Forbes, J.W. (Eds.), Shock Compression of Condensed Matter. American Institute of Physics, pp. 517-520.

Baer, M.R., Trott, W.M., 2005. Theoretical and experimental mesoscale studies of impact-loaded granular explosive and simulant materials. In: Proceedings of the 12th International Symposium on Detonation. Office of Naval Research, 333-05-2, pp. 939-948.

Baoping, Z., Chao, Y., Yingming, X., Chunlan, J., 1994. Responsive behaviour of 93 wt. % tungsten alloy under intense shock loading. In: Zhemin, Z., Quinming, T. (Eds.), Proc. IUTAM Symposium on Impact Dynamics. Peking University Press, pp. 283-297.

Barker, L.M., 2000. The development of the VISAR, and its use in shock compression science. In: Furnish, M.D., Chhabildas, L.C., Hixson, R.S. (Eds.), Shock Compression of Condensed Matter. American Institute of Physics, pp. 11-17.

Batra, R.C., Love, B.M., 2005. Crack propagation due to brittle and ductile failures in microporous thermoelasticviscoplastic functionally graded materials. Engineering Fracture Mechanics 72, 1954-1979.

Batra, R.C., Love, B.M., 2006a. Consideration of microstructural effects in the analysis of adiabatic shear bands in a tungsten heavy alloy. International Journal of Plasticity 22, 1858-1878.

Batra, R.C., Love, B.M., 2006b. Multiscale analysis of adiabatic shear bands in tungsten heavy alloy particulate composites. International Journal of Multiscale Computational Engineering 4, 95-114.

Baumung, K., Singer, J., Razorenov, S.V., Utkin, A.V., 1996. Hydrodynamic proton beam-target interaction experiments using an improved line-imaging velocimeter. In: Schmidt, S.C., Tao, W.C. (Eds.), Shock Compression of Condensed Matter. American Institute of Physics, pp. 1015-1018.

Becker, R., 2004. Effects of crystal plasticity on materials loaded at high pressures and strain rates. International Journal of Plasticity 20, 1983-2006.

Bless, S., Chau, R., 2006. Tensile failure of tungsten rods. In: Furnish, M.D., Elert, M., Russell, T.P., White, C.T. (Eds.), Shock Compression of Condensed Matter. American Institute of Physics, pp. 603-606.

Bless, S.J., Tarcza, K., Chau, R., Taleff, E., Persad, C., 2006. Dynamic fracture of tungsten heavy alloys. International Journal of Impact Engineering 33, 100-108.

Bloomquist, D.D., Sheffield, S.A., 1983. Optically recording interferometer for velocity measurements with subnanosecond resolution. Journal of Applied Physics 54, 1717-1722.

Brannon, P.J., Konrad, C.H., Morris, R.W., Jones, E.D., Asay, J.R., 1983. Studies of the spectral and spatial characteristics of shock-induced luminescence from x-cut quartz. Journal of Applied Physics 54, 6474-6381.

Brannon, R.M., Strack, O.E., Lee, M.Y., 2007. Spatial statistics of material strength to address mesh dependency of conventional damage models. Part I: theory and experiments. (in preparation).

Bury, K.V., 1975. Statistical Models in Applied Science. Wiley, New York, chapter 12.

Case, S., Horie, Y., 2006. Discrete element simulation of shock wave propagation in polycrystals. Journal of the Mechanics and Physics of Solids, submitted.

Chhabildas, L.C., Trott, W.M., Reinhart, W.D., Cogar, J.R., Mann, G.A., 2002. Incipient spall studies in tantalum - microstructural effects. In: Furnish, M.D., Thadhani, N.N., Horie, Y. (Eds.), Shock Compression of Condensed Matter. American Institute of Physics, pp. 483-486.

Clayton, J.D., 2005a. Dynamic plasticity and fracture in high density polycrystals: constitutive modeling and numerical simulation. Journal of the Mechanics and Physics of Solids 53, 261-301.

Clayton, J.D., 2005b. Modeling dynamic plasticity and spall fracture in high density polycrystalline alloys. International Journal of Solids and Structures 42, 4613-4640.

Clayton, J.D., 2006a. Continuum multiscale modeling of finite deformation plasticity and anisotropic damage in polycrystals. Theoretical and Applied Fracture Mechanics 45, 163-185.

Clayton, J.D., 2006b. Plasticity and spall in high density polycrystals: modeling and simulation. In: Furnish, M.D., Elert, M., Russell, T.P., White, C.T. (Eds.), Shock Compression of Condensed Matter. American Institute of Physics, pp. 311-314.

Dandekar, D.P., 2004. Spall strength of silicon carbide under normal and simultaneous compression-shear shock wave loading. International Journal of Applied Ceramics Technology 1, 261-268.

Dandekar, D.P., Weisgerber, W.J., 1999. Shock response of a heavy tungsten alloy. International

Journal of Plasticity 15, 1291-1309.

Espinosa, H.D., Zavattieri, P.D., 2003a. A grain level model for the study of failure initiation and evolution in polycrystalline brittle materials. Part I: Theory and numerical implementation. Mechanics of Materials 35, 333-364.

Espinosa, H.D., Zavattieri, P.D., 2003b. A grain level model for the study of failure initiation and evolution in polycrystalline brittle materials. Part II: numerical examples. Mechanics of Materials 35, 365-394.

Furnish, M.D., Reinhart, W.D., Trott, W.M., Chhabildas, L.C., Vogler, T.J., 2006. Variability in dynamic properties of tantalum: spall, Hugoniot elastic limit, and attenuation. In: Furnish, M.D., Elert, M., Russell, T.P., White, C.T. (Eds.), Shock Compression of Condensed Matter. American Institute of Physics, pp. 615-618.

Furnish, M.D., Trott, W.M., Mason, J., Podsednik, J., Reinhart, W.D., Hall, C.A., 2004. Assessing mesoscale material response via high-resolution line-imaging VISAR. In: Furnish, M.D., Gupta, Y.M., Forbes, J.W. (Eds.), Shock Compression of Condensed Matter. American Institute of Physics, pp. 1159-1162.

Goto, D., Orzechowski, T., Becker, R., 2007. personal communication.

Hirth, J.P., Lothe, J., 1982. Theory of Dislocations. Krieger, Malabar, FL

Johnson, G.R., 1981. Dynamic analysis of a torsion test specimen including heat conduction and plastic flow. ASME Journal of Engineering Materials and Technology 103, 201-206.

Johnson, G.R., Stryk, R.A., Beissel, S.R., 2001. User instructions for the 2001 version of the EPIC code. Alliant Techsystems, Hopkins, MN. (Distribution authorized to U.S. government agencies and their contractors only.)

Kim, D.S., Nemat-Nasser, S., Isaacs, J.B., Lischer, D., 1998. Adiabatic shearband in WHA in high-strain-rate compression. Mechanics of Materials 28, 227-236.

Kocks, U.F., Tomé, C.N., Wenk, H.-R., 1998. Texture and Anisotropy: Preferred Orientations in Polycrystals and their Effect on Material Properties. Cambridge University Press, Cambridge, U.K.

Love, B.M., Batra, R.C., 2005. Determination of effective thermomechanical parameters of a mixture of two elastothermoviscoplastic constituents. International Journal of Plasticity 22, 1026-1061.

Lu, C., Danzer, R., Fischer, F.D., 2002. Fracture statistics of brittle materials: Weibull or normal distribution. Physical Review E 65, 067102.

Magness, L.S., 1994. High strain rate deformation behaviors of kinetic energy penetrator materials during ballistic impact. Mechanics of Materials 17, 147-154.

Margetson, J., Sherwood, P.J., 1979. Statistical analysis of the brittle fracture of sintered tungsten. Journal of Materials Science 14, 2575-2580.

McMillan, C.F., Goosman, D.R., Parker, N.L., Steinmetz, L.L., Chau, H.H., Huen, T., Whipkey, R.K., Perry, S.J., 1988. Velocimetry of fast surfaces using Fabry-Perot interferometry. Review of Scientific Instruments 59, 1-20.

Mescheryakov, Y.I., 2003. Meso-macro energy exchange in shock deformed and fractured solids. In: Horie, Y., Davison, L., Thadhani, N.N. (Eds.), High-Pressure Shock Compression of Solids VI: Old Paradigms and New Challenges. Springer-Verlag, New York, pp. 169-213.

Mescheryakov, Y.I., Atroshenko, S.A., 1992. Multiscale rotations in dynamically deformed solids. International Journal of Solids and Structures 29, 2761-2778.

Mescheryakov, Y.I., Divakov, A.K., N.I., Z., 2004. Shock-induced structural transitions and dynamic strength of solids. International Journal of Solids and Structures 41, 2349-2362.

Meyers, M.A., Carvalho, M.S., 1976. Shock-front irregularities in polycrystalline metals. Materials Science and Engineering 24, 131-135.

Millett, J.C.F., Bourne, N.K., Rosenberg, Z., Field, J.E., 1999. Shear strength measurements in a tungsten alloy during shock loading. Journal of Applied Physics 86, 6707-6709.

Nemat-Nasser, S., Okinaka, T., Ni, L., 1998. A physically-based constitutive model for BCC crystals with application to polycrystalline tantalum. Journal of the Mechanics and Physics of Solids 46, 1009-1038.

Ramesh, K.T., Coates, R.S., 1992. Microstructural influences on the dynamic response of tungsten heavy alloys. Metallurgical Transactions 23A, 2625-2630.

Reinhart, W.D., Chhabildas, L.C., Trott, W.M., Dandekar, D.P., 2002. Investigating multi-dimensional effects in single-crystal sapphire. In: Furnish, M.D., Thadhani, N.N., Horie, Y. (Eds.), Shock Compression of Condensed Matter. American Institute of Physics, pp. 791-794.

Ruoff, A.L., Rodriguez, C.O., Christensen, N.E., 1998. Elastic moduli of tungsten to 15 Mbar, phase transition to 6.5 Mbar, and rheology to 6 Mbar. Physical Review B 58, 2998-3002.

Schoenfeld, S.E., 1998. Dynamic behavior of polycrystalline tantalum. International Journal of Plasticity 14, 871-890.

Schoenfeld, S.E., Kad, B.K., 2002. Texture effects on shear response in Ti-6Al-4V plates. International Journal of Plasticity 18, 461-486.

Schraml, S.J., Meyer, H.W., Kleponis, D.S., Kimsey, K.D., 2005. Simulating the formation and evolution of behind armor debris fields. In: Proceedings 2005 DoD High Performance Computing Users Group Conference.

Subhash, G., Lee, Y.J., Ravichandran, G., 1994. Plastic deformation of CVD textured tungsten -

I. constitutive response. Acta Metallurgica et Materialia 42, 319-330.

Trott, W.M., Asay, J.R., 1998. Investigation of microscale shock phenomena using a line-imaging optical recording velocity interferometer system. In: Schmidt, S.C., Dandekar, D.P., Forbes, J.W. (Eds.), Shock Compression of Condensed Matter. American Institue of Physics, pp. 837-840.

Trott, W.M., Baer, M.R., Castañeda, J.N., Chhabildas, L.C., Asay, J.R., 2006. Investigation of the mesoscopic scale response of low-density pressings of granular sugar under impact. Journal of Applied Physics, submitted.

Trott, W.M., Baer, M.R., Castañeda, J.N., Tappan, A.S., Stuecker, J.N., Cesarano, J., 2007. Shock-induced reaction in a nitromethane-impregnated geometrically regular sample configuration. In: Proceedings of the 13th International Detonation Symposium (in press).

Trott, W.M., Castañeda, J.N., O'Hare, J.J., Knudson, M.D., Chhabildas, L.C., Baer, M.R., Asay, J.R., 2001. Examination of the mesoscopic scale response of shock compressed heterogeneous materials using a line-imaging velocity interferometer. In: Staudhammer, K.P., Murr, L.E., Meyers, M.A. (Eds.), Fundamental Issues and Applications of Shock-Wave and High-Strain-Rate Phenomena. Elsevier, pp. 647-654.

Trott, W.M., Chhabildas, L.C., Baer, M.R., Castañeda, J.N., 2002. Investigation of dispersive waves in low-density sugar and HMX using line-imaging velocity interferometry. In: Furnish, M.D., Thadhani, N.N., Horie, Y. (Eds.), Shock Compression of Condensed Matter. American Institute of Physics, pp. 845-848.

Trott, W.M., Knudson, M.D., Chhabildas, L.C., Asay, J.R., 2000. Measurements of spatially resolved velocity variations in shock compressed heterogeneous materials using a line-imaging velocity interferometer. In: Furnish, M.D., Chhabildas, L.C., Hixson, R.S. (Eds.), Shock Compression of Condensed Matter. American Institute of Physics, pp. 993-998.

Vogler, T.J., Reinhart, W.D., Chhabildas, L.C., 2004. Dynamic behavior of boron carbide. Journal of Applied Physics 95, 4173-4183.

Weerasooriya, T., 2003. Deformation and failure behavior of a tungsten heavy alloy under tensile loading at different strain rates. In: Proceedings of the SEM Annual Conference on Experimental Mechanics.

Weerasooriya, T., Beaulieu, P.A., 1993. Effects of strain rate on the deformation and failure behavior of 93W-5Ni-2Fe under shear loading. Materials Science and Engineering A172, 71-78.

Weerasooriya, T., Moy, P., Dowding, R., 1994. Effect of W-W contiguity on the high shear strain rate behavior of 93W-5Ni-2Fe tungsten heavy alloy. In: Bose, A., Dowding, R. (Eds.), Proceedings of the 2nd International Conference on Tungsten and Refractory Metals. Metal Powder Industries, pp. 401-409.

Weibull, W., 1951. A statistical distribution function of wide applicability. Journal of Applied Mechanics 18, 293-297.

Yano, K., Horie, Y., 1999. Discrete-element modeling of shock compression of polycrystalline copper. Physical Review B 59, 13672-13680.

Yano, K., Horie, Y., 2002. Mesomechanics of the α-β transition in iron. International Journal of Plasticity 18, 1427-1446.

Zhou, F., Molinari, J.-F., 2004. Stochastic fracture of ceramics under dynamic tensile loading. International Journal of Solids and Structures 41, 6573-6596.

Zhou, M., 1998a. Effects of microstructure on resistance to shear localization for a class of metal matrix composites. Fatigue and Fracture of Engineering Materials and Structures 21, 425-438.

Zhou, M., 1998b. Growth of shear bands in composite microstructures. International Journal of Plasticity 14, 733-754.

Zhou, M., Clifton, R.J., 1997. Dynamic constitutive and failure behavior of a two-phase tungsten composite. Journal of Applied Mechanics 64, 487-494.

Zhou, M., Clifton, R.J., Needleman, A., 1994. Finite element simulations of shear localization in plate impact. Journal of the Mechanics and Physics of Solids 42, 423-458.

Zurek, A.K., Gray, G.T., 1991. Dynamic strength and strain rate effects on fracture behavior of tungsten and tungsten alloys. Journal de Physique IV C3, 631-637.

Tables

Table 1 Details of plate impact experiments.

Expt.	**Sample Orient.**	**Impactor/target thickness [mm]**	**V_I [km/s]**	**HEL [GPa]**	**U_s^p [km/s]**	**σ_h [GPa]**	**ρ_h [g/cm^3]**
WHA-1	axial	1.54 / 3.07	0.249	2.54	4.20	-9.63	18.27
WHA-2	axial	1.54 / 3.06	0.345	2.40	4.27	-13.35	18.48
WHA-3	transverse	1.47 / 2.96	0.246	0.83	4.20	-9.31	18.30
WHA-4	transverse	1.48 / 2.95	0.347	4.09	4.10	-13.16	18.53
WHA-5	transverse	1.48 / 2.95	0.426	2.86	4.06	-15.81	18.73

Table 2 Thermoelastic properties for tungsten and matrix materials.

Property	**Value (W)**	**Value (Matrix)**
μ [GPa]	$160.3 - 0.0146(\Delta\theta) - 3.3\text{x}10^{-6}(\Delta\theta)^2$	99.0
K_o [GPa]	$310.8 - 0.01759(\Delta\theta) - 3\text{x}10^{-7}(\Delta\theta)^2$	190.3
K_1 [GPa]	1450	--
α_T [K^{-1}]	$5.3\text{x}10^{-6} + 1.584\text{x}10^{-9}(\Delta\theta)$	$1.5\text{x}10^{-5}$
$\hat{c}$ [J kg^{-1} K^{-1}]	$135.8(1-4805/\theta^2) + 0.00912\theta + 2.31\text{x}10^{-9}\theta^3$	382
k [W m^{-1} K^{-1}]	$160 - 0.05(\Delta\theta)$	100
ρ_o [kg/m^3]	19350	9200

Table 3 Properties for inelastic material response of tungsten and matrix.

Parameter	Value (W)	Value (Matrix)
$\dot{\gamma}_0$ [s^{-1}]	0.001	0.001
m	20	20
q	1.4	1.0
A [MPa]	630	200
B	1.5	0.4
$g_y^{(\alpha)}$ [MPa]	500	150
p	-1.5	-1.5
θ_o [K]	300	300
$\hat{\alpha}$	0.439	1.03
b [nm]	0.275	0.257
κ	1333	200

Table 4 Properties for interfacial fracture.

Parameter	Value
$\hat{s}_0$ [GPa]	2.0
$\hat{s}_1$ [GPa/K]	0.01
$\hat{\tau}_0$ [GPa]	4.0
$\hat{\tau}_1$ [GPa/K]	0.01
δ_c [μm]	1.0

Table 5 Numerical simulations.

Simulation	**Orientation**	V_I **(m/s)**
WHA-I	axial	350
WHA-II	transverse-1	350
WHA-III	transverse-2	250
WHA-IV	transverse-2	350
WHA-V	transverse-1	450

Table 6 Statistical parameters for experimental spall strengths.

			Normal Distribution		Weibull Distribution	
Expt.	U_t **[km/s]**	$\sigma_{sp}\left(\bar{u}_p\right)$ **[GPa]**	$\bar{\sigma}_{sp}$ **[GPa]**	$S(\sigma_{sp})$ **[GPa]**	σ_o **[GPa]**	β
WHA-1	4.34	1.62	1.85	0.31	1.98	6.92
WHA-2	4.62	2.01	2.13	0.37	2.29	6.13
WHA-3	4.48	1.55	1.66	0.32	1.79	6.00
WHA-4	4.70	1.55	1.70	0.33	1.84	4.99
WHA-5	4.36	1.59	1.98	0.61	2.20	3.46

Table 7 Statistical parameters for spall from simulations.

		Normal Distribution		Weibull Distribution	
Expt.	$\sigma_{sp}\left(\bar{u}_p\right)$ **[GPa]**	$\bar{\sigma}_{sp}$ **[GPa]**	$S(\sigma_{sp})$ **[GPa]**	σ_o **[GPa]**	β
WHA-I	1.91	2.00*	0.31	2.12	8.74
WHA-II	2.77	2.88	0.18	2.96	18.77
WHA-III	1.39	1.57	0.14	1.63	11.28
WHA-IV	1.29	1.50	0.20	1.59	7.82
WHA-VI	2.57	2.69	0.18	2.77	14.89

*Used to determine a single impedance value for all simulations.

FIGURE CAPTIONS

Fig. 1 Micrograph showing WHA microstructure (image courtesy of T. Weerasooriya, ARL).

Fig. 2 Schematic of sample orientations relative to penetrator axis and anisotropic WHA microstructure. W grains colored by lattice orientation from EBSD scans.

Fig. 3 Set-up for plate impact experiments.

Fig. 4 Finite element meshes used in simulations.

Fig. 5 Streak camera record from line-VISAR for experiment WHA-2.

Fig. 6 Free surface velocity history for experiment WHA-2.

Fig. 7 Free surface velocity history for experiment WHA-2: spatial average (black), spatial variation (red), and standard deviation (blue, magnified10×).

Fig. 8 Contours of constant free surface velocity of shock front in *y-t* plane for experiment WHA-2.

Fig. 9 Perturbations of free surface velocity for experiment WHA-2.

Fig. 10 Spatially-averaged free surface velocity histories for all experiments.

Fig. 11 Standard deviation in free surface velocities for experiments WHA 1-4.

Fig. 12 Contours of constant free surface velocity ($V_I/2$) of shock front in *y-t* plane for experiments WHA 1-4.

Fig. 13 Overall compressive stress - engineering strain response for current experiments and from Dandekar & Weisgerber (1999).

Fig. 14 Schematic of wave propagation in a plate impact experiment.

Fig. 15 Schematic of average stress states in target material during a plate impact experiment.

Fig. 16 Spatially resolved peak particle velocity (u_1-blue), pullback velocity (u_2-red), and their difference (Δu_{FS}-black) for experiment WHA-2.

Fig. 17 Probability distribution of spall strength and Weibull fit for experiment WHA-2.

Fig. 18 Field variables for simulation WHA-III at t = 40 ns (~ initiation of spall): (a) pressure, (b) elastic energy density, (c) cumulative plastic strain, and (d) dislocation density.

Fig. 19 Field variables for simulation WHA-IV at t = 40 ns (~ initiation of spall): (a) pressure, (b) elastic energy density, (c) cumulative plastic strain, and (d) dislocation density.

Fig. 20 Effective stress near spall planes at t = 60 ns from simulations (a) WHA-I, (b) WHA-II, (c) WHA-III, (d) WHA-IV, and (e) WHA-V.

Fig. 21 Effective stress near spall planes at t = 80 ns from simulations (a) WHA-I, (b) WHA-II, (c) WHA-III, (d) WHA-IV, and (e) WHA-V.

Fig. 22 Cumulative damage from microcracking: (a) summed product of crack length and opening displacement and (b) density of fully opened cracks ($\delta \geq \delta_c$).

Fig. 23 Free surface velocity history from simulation WHA-IV.

Fig. 24 Perturbations of free surface velocity from simulation WHA-IV.

Fig. 25 Contours of constant free surface velocity of shock front in y-t plane from simulation WHA-IV.

Fig. 26 Spatially-averaged free surface velocity histories for all simulations.

Fig. 27 Standard deviation in free surface velocities from simulations.

Fig. 28 Contours of constant free surface velocity ($V_I/2$) of shock front in y-t plane for simulations WHA I-V.

Fig. 29 (a) Particle velocity $\boldsymbol{u_p}$ (arrows are velocity vectors; colors indicate velocity magnitude) and (b) effective stress σ^{eff} at 20 ns for simulation WHA-I.

Fig. 30 (a) Particle velocity $\boldsymbol{u_p}$ (arrows are velocity vectors; colors indicate velocity magnitude) and (b) effective stress σ^{eff} at 20 ns for simulation WHA-IV.

Figure 1

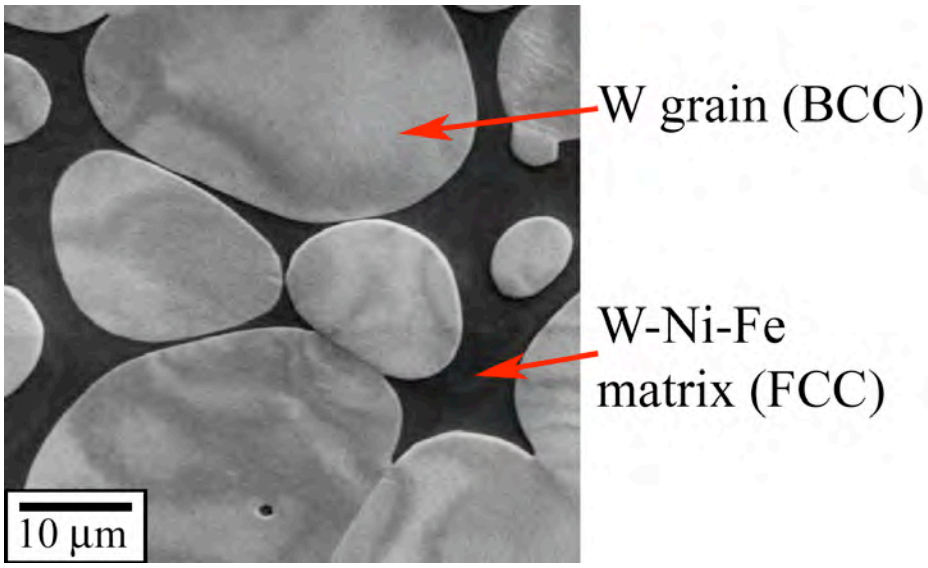

Figure 2

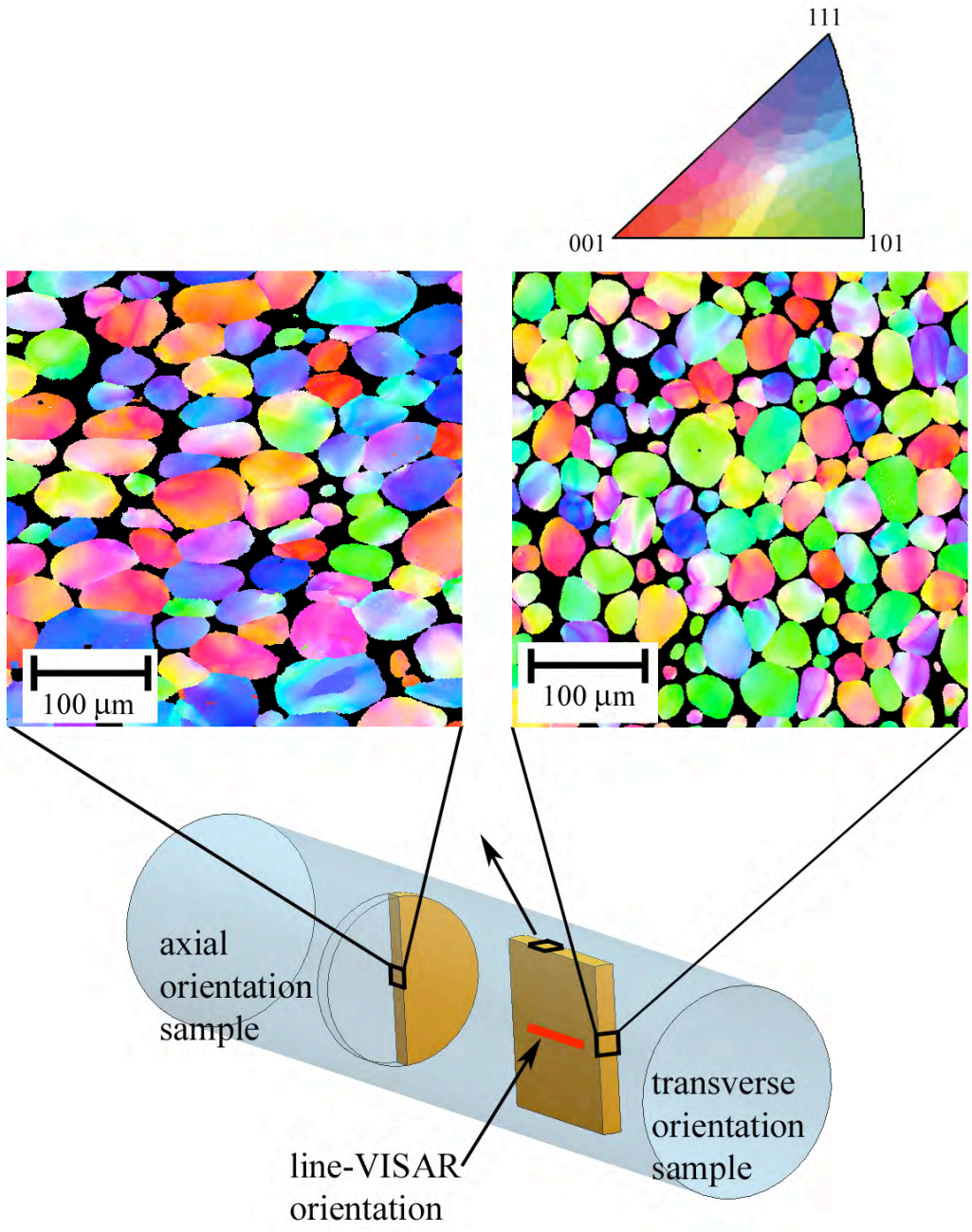
111
001
101
100 µm
100 µm
axial
orientation
sample
transverse
orientation
sample
line-VISAR
orientation

Figure 3

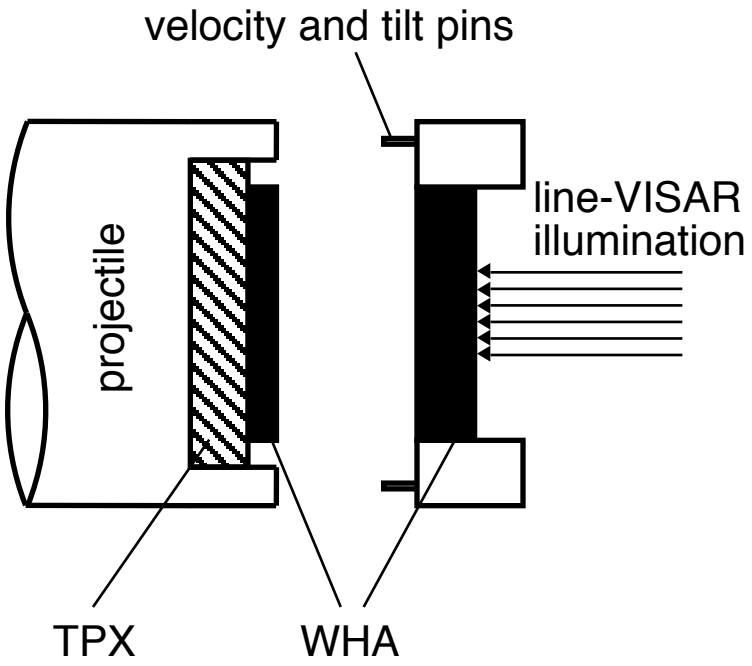
velocity and tilt pins
line-VISAR
illumination
projectile
TPX
WHA

Figure 4

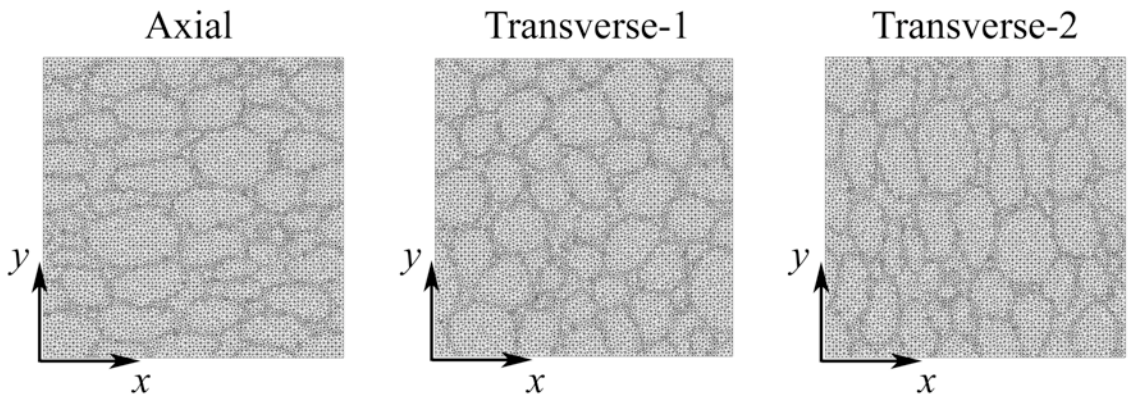

Figure 5

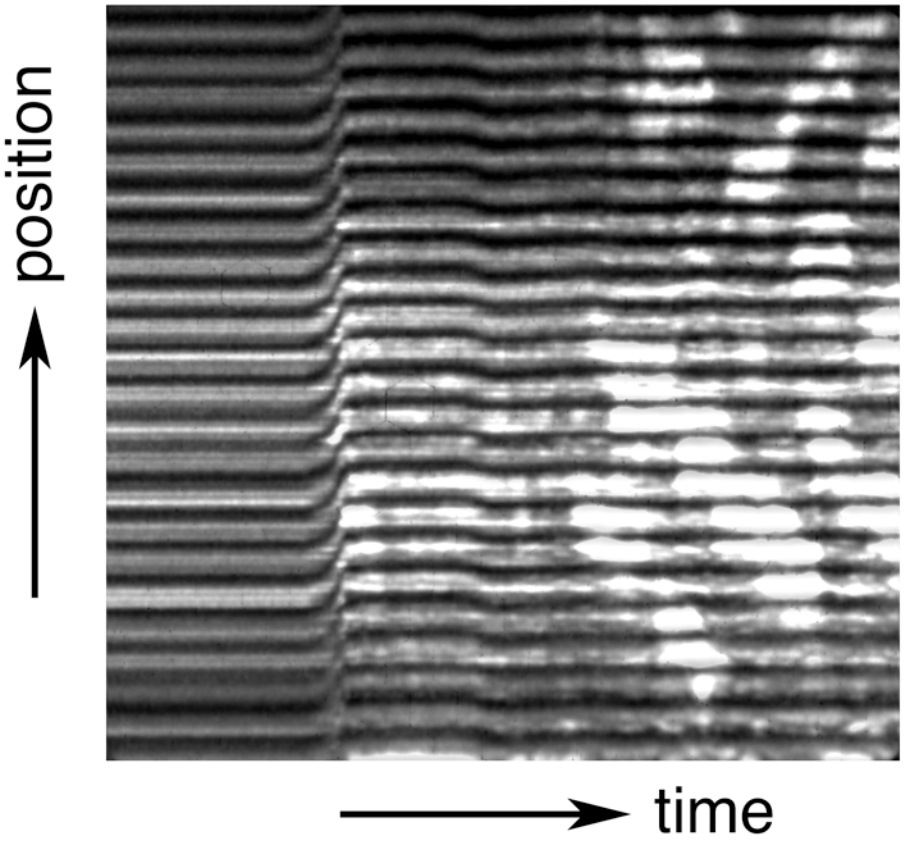

Figure 6

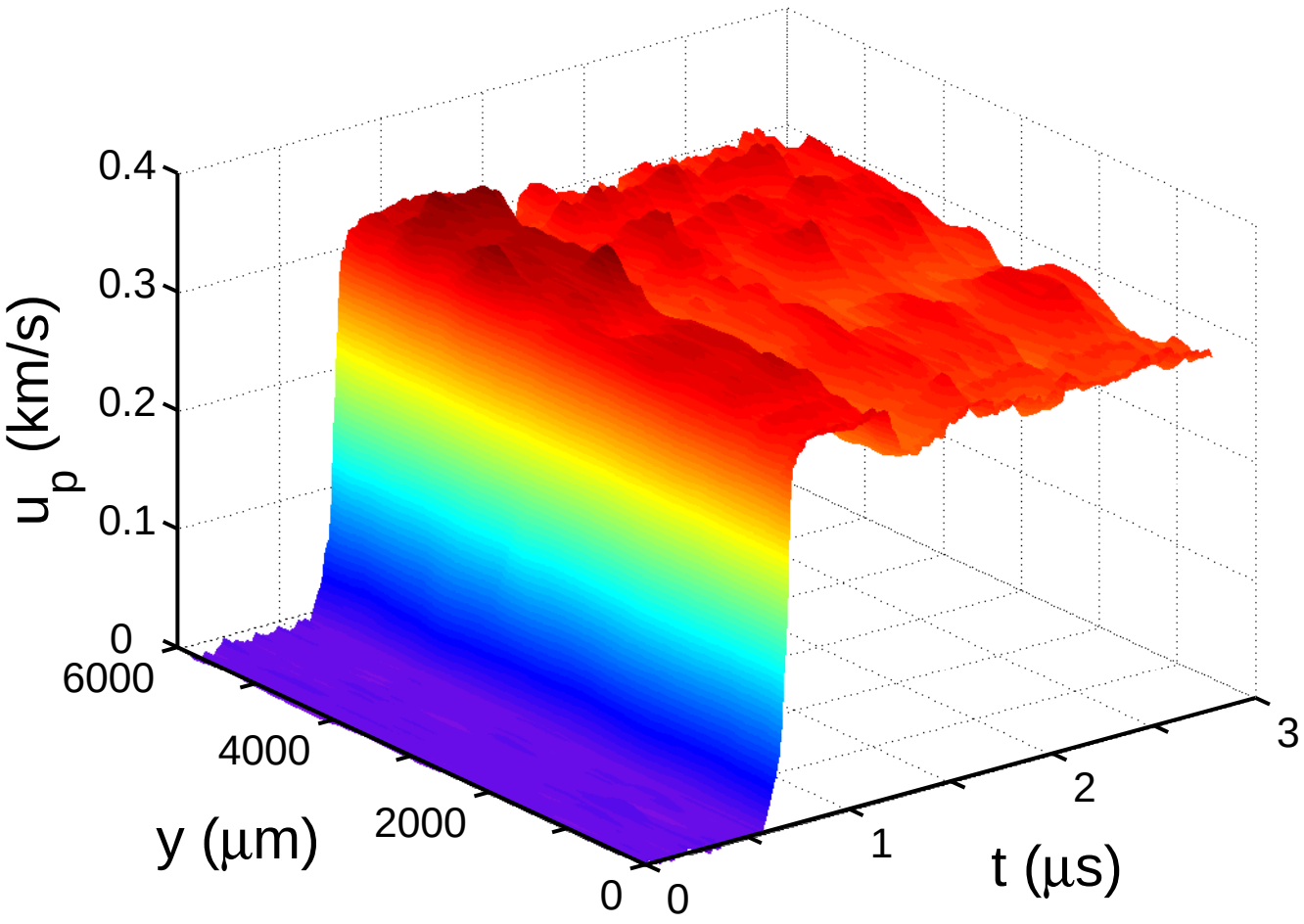

Figure 7

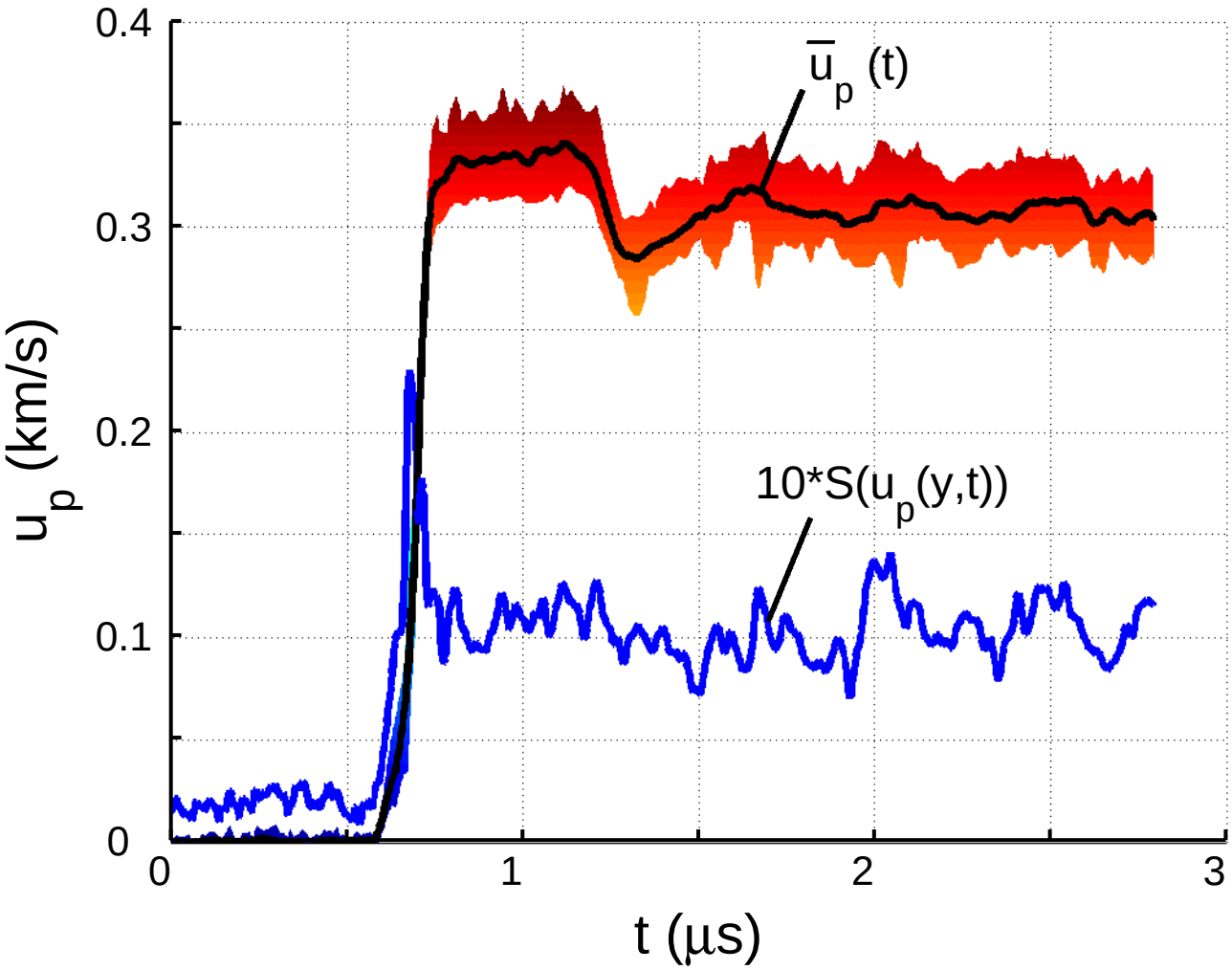

Figure 8

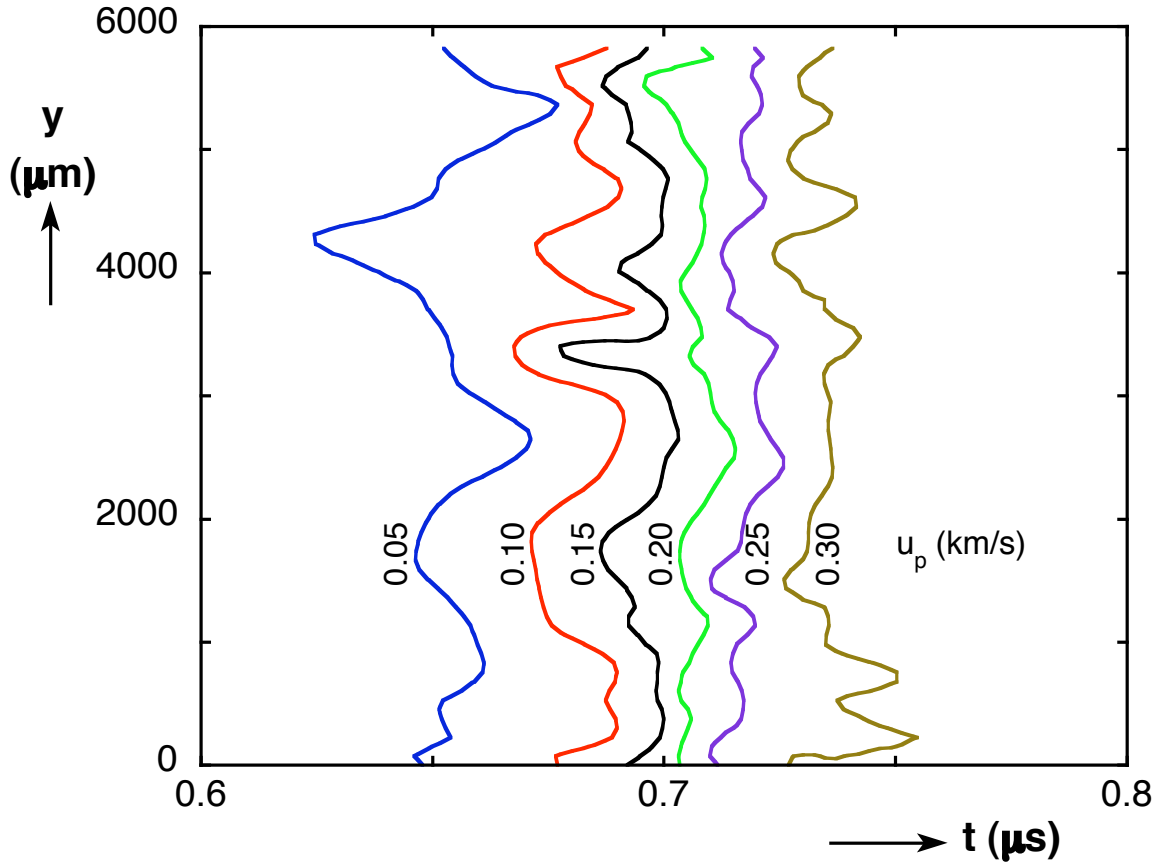

Figure 9

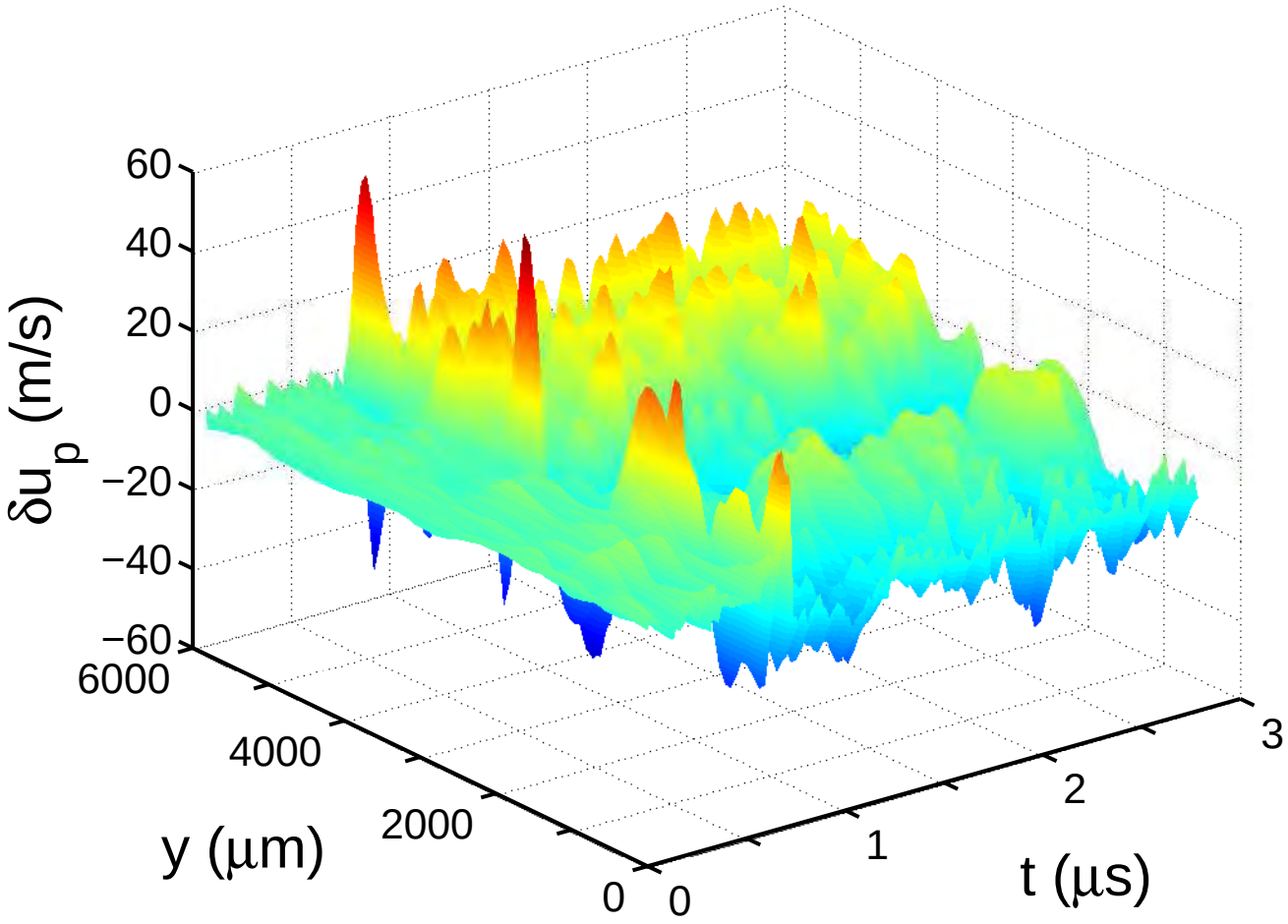

Figure 10

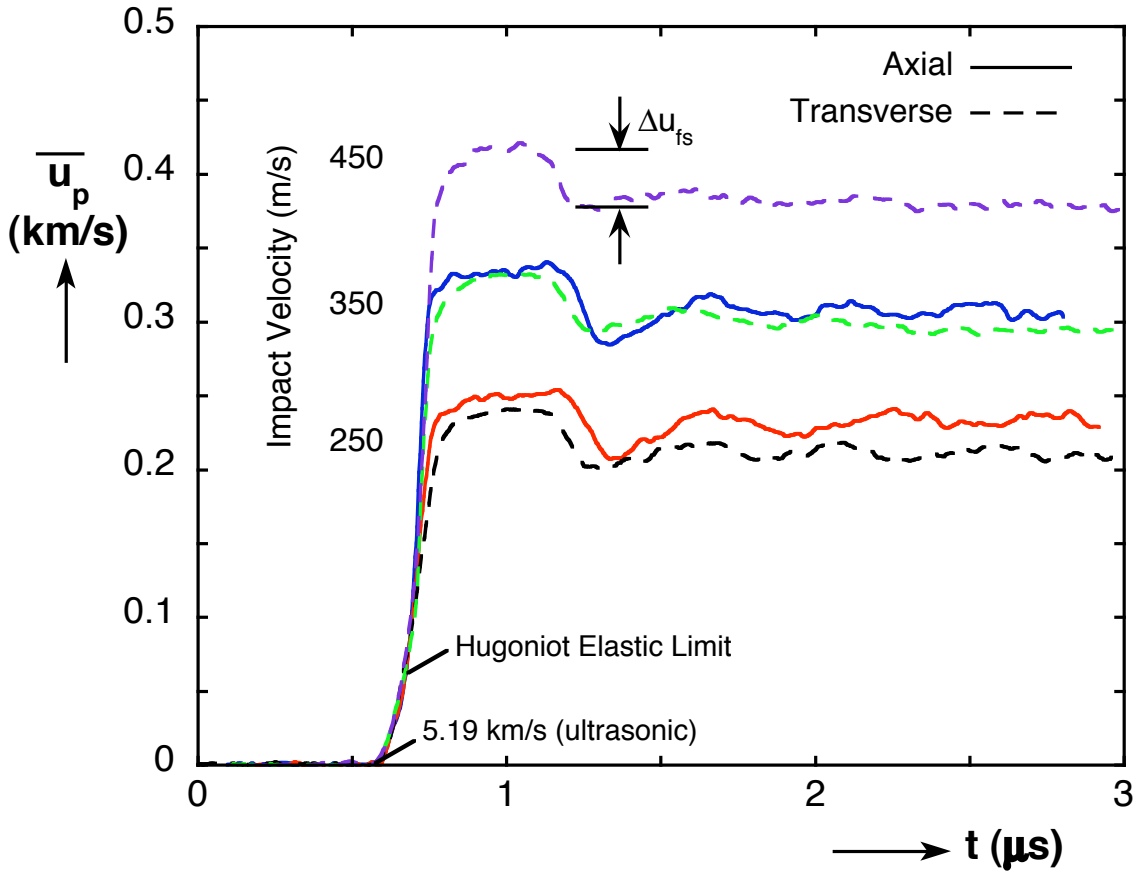
0.5
0.4
0.3
0.2
0.1
0
$\overline{u_p}$ (km/s)
Impact Velocity (m/s)
450
350
250
Axial
Transverse
Δu_{fs}
Hugoniot Elastic Limit
5.19 km/s (ultrasonic)
0
1
2
3
t (μs)

Figure 11

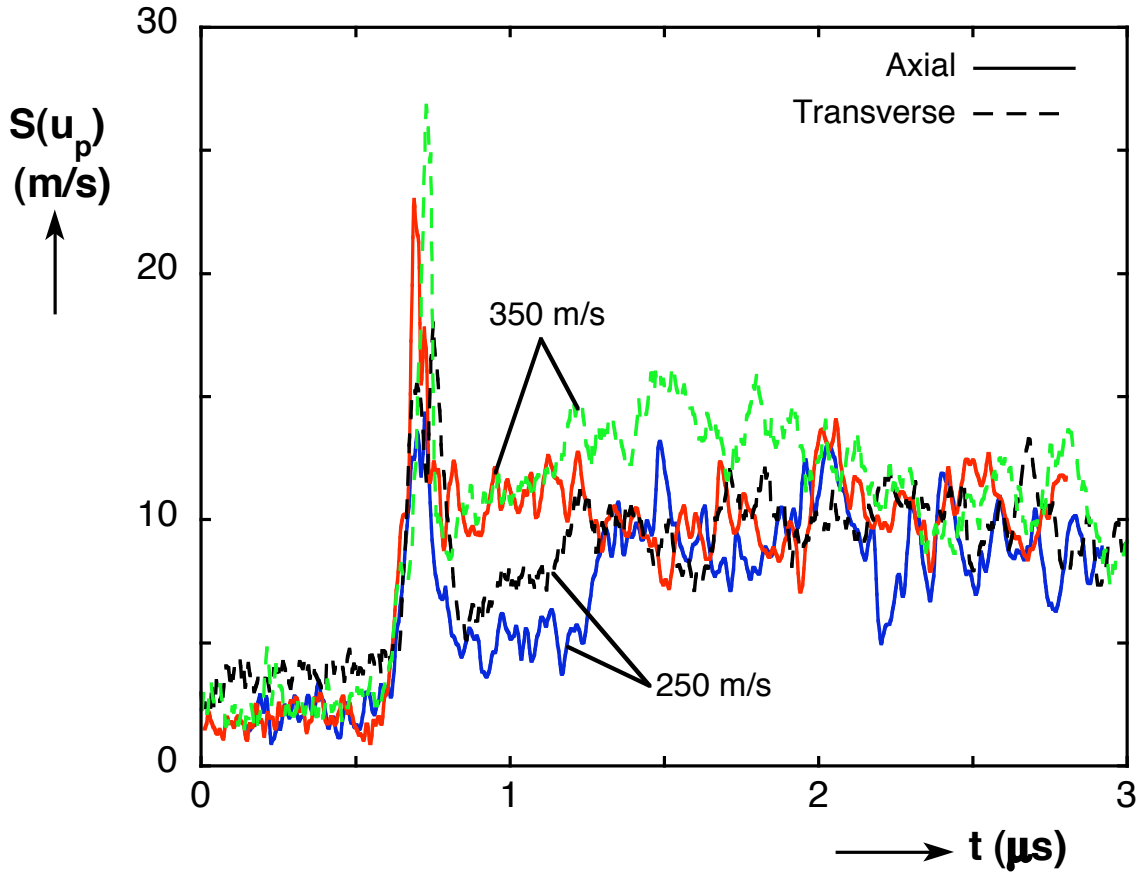

Figure 12

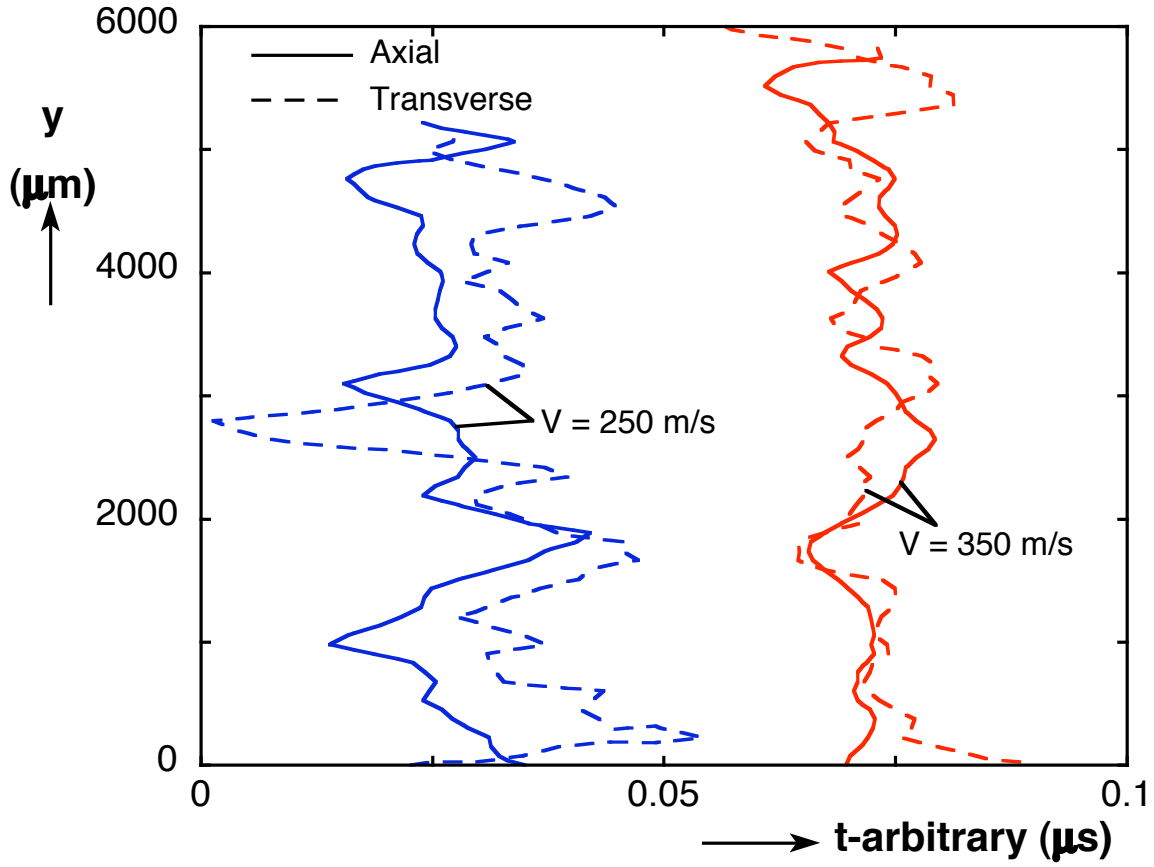
6000
4000
2000
0
y
(µm)
Axial
Transverse
V = 250 m/s
V = 350 m/s
0
0.05
0.1
t-arbitrary (µs)

Figure 13

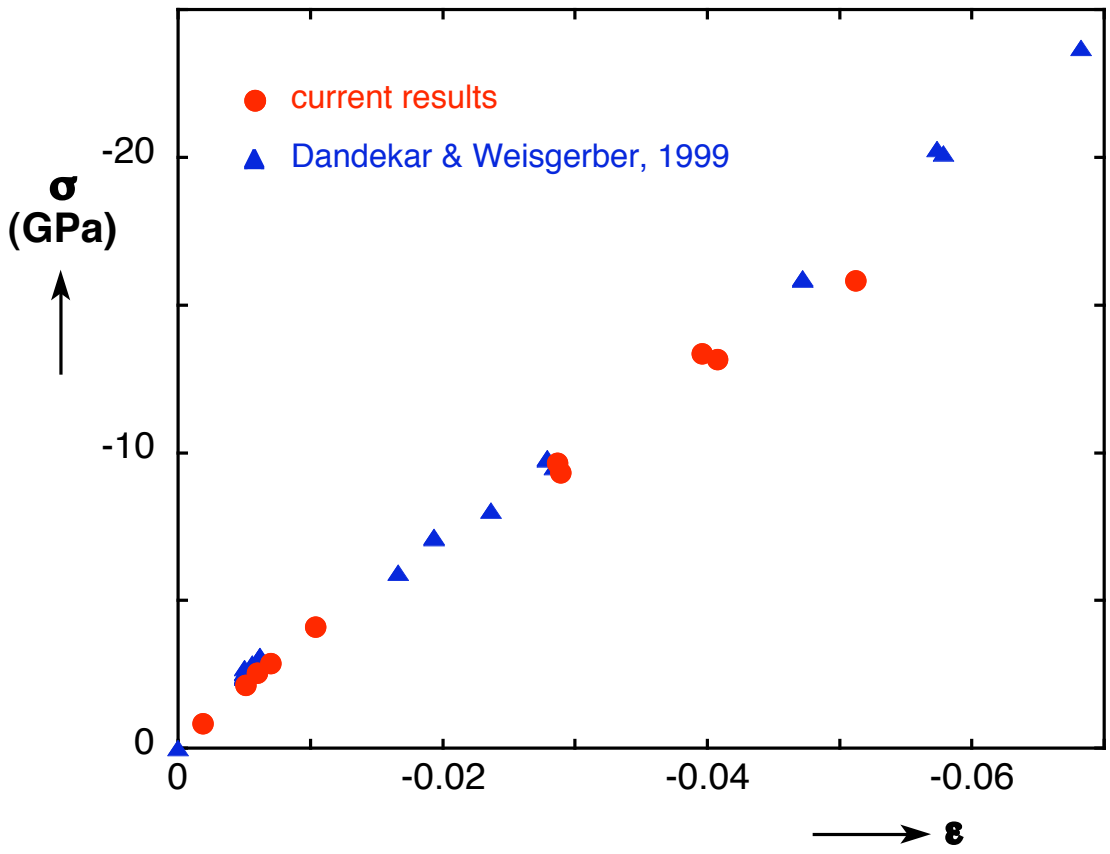
current results
Dandekar & Weisgerber, 1999
σ
(GPa)
-20
-10
0
0
-0.02
-0.04
-0.06
ε

Figure 14

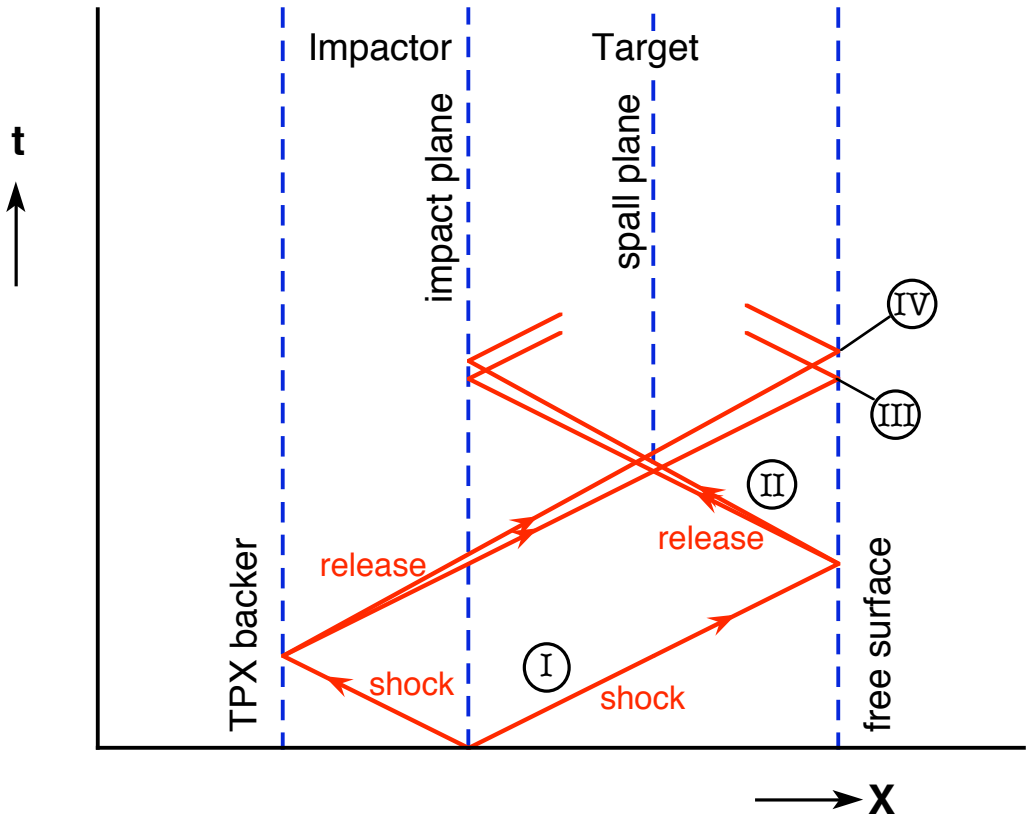
t
Impactor
Target
impact plane
spall plane
IV
III
II
release
release
TPX backer
shock
I
shock
free surface
X

Figure 15

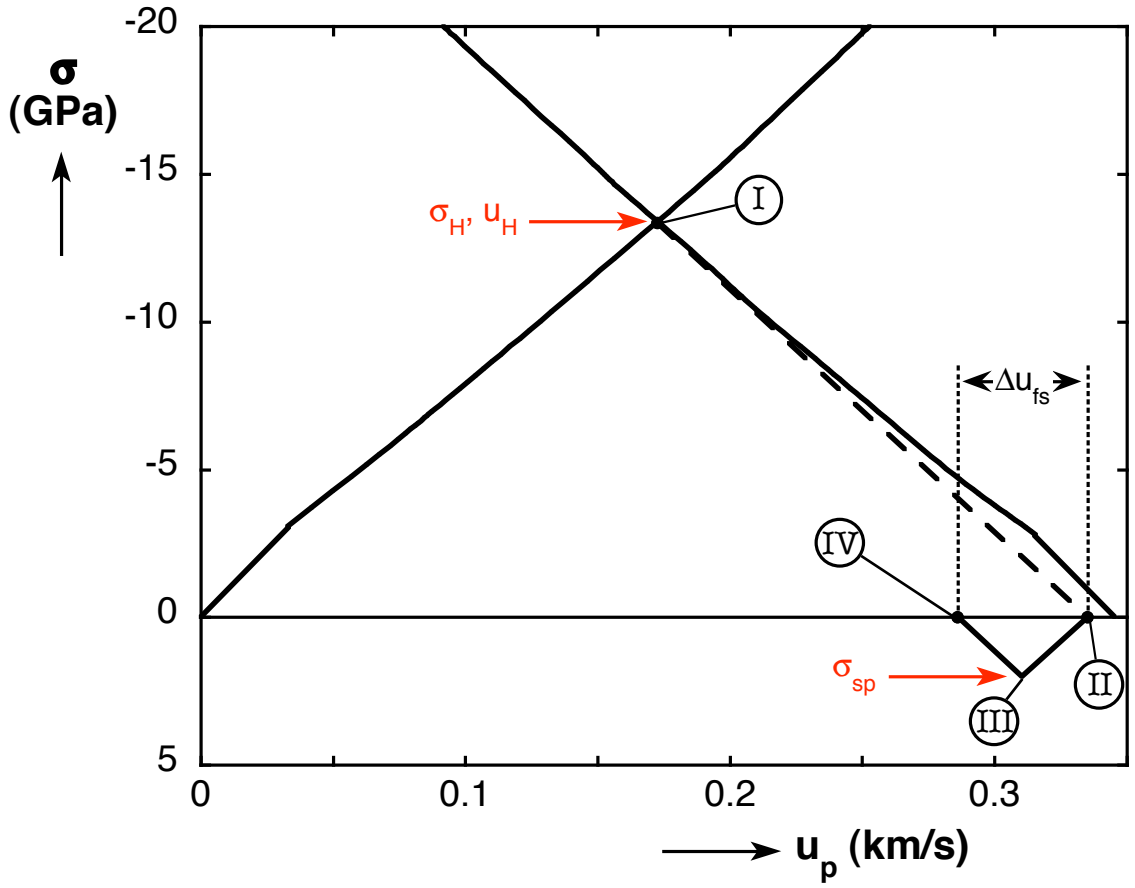

Figure 16

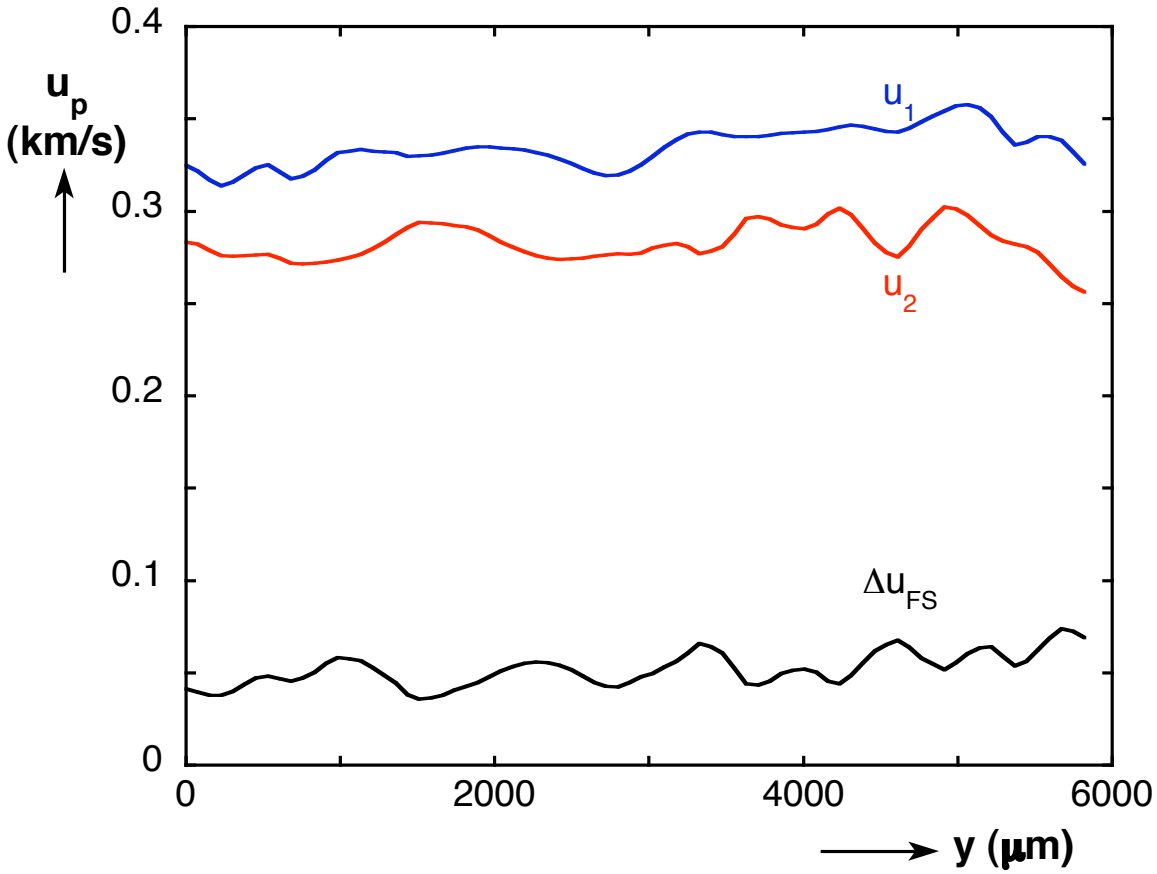

Figure 17

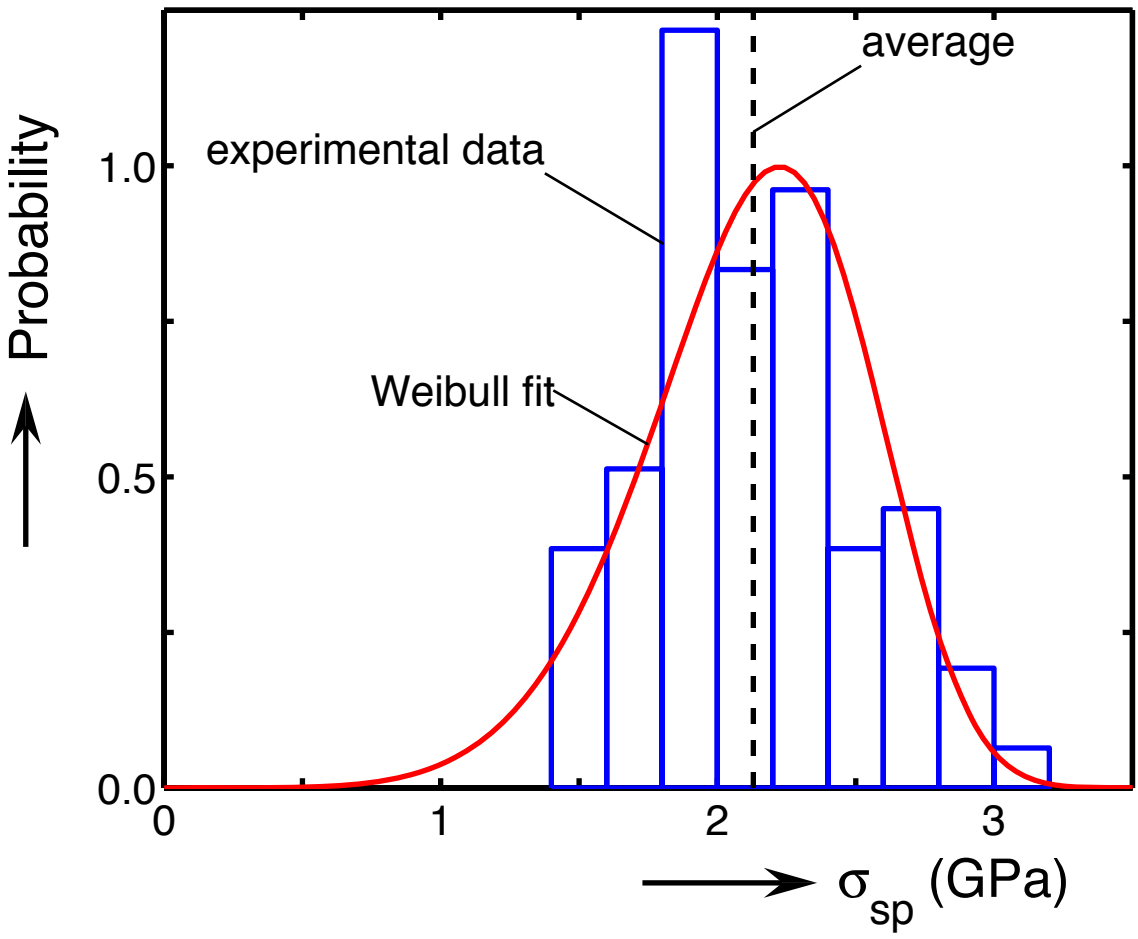
Probability
1.0
0.5
0.0
0
1
2
3
average
experimental data
Weibull fit
σsp (GPa)

Figure 18

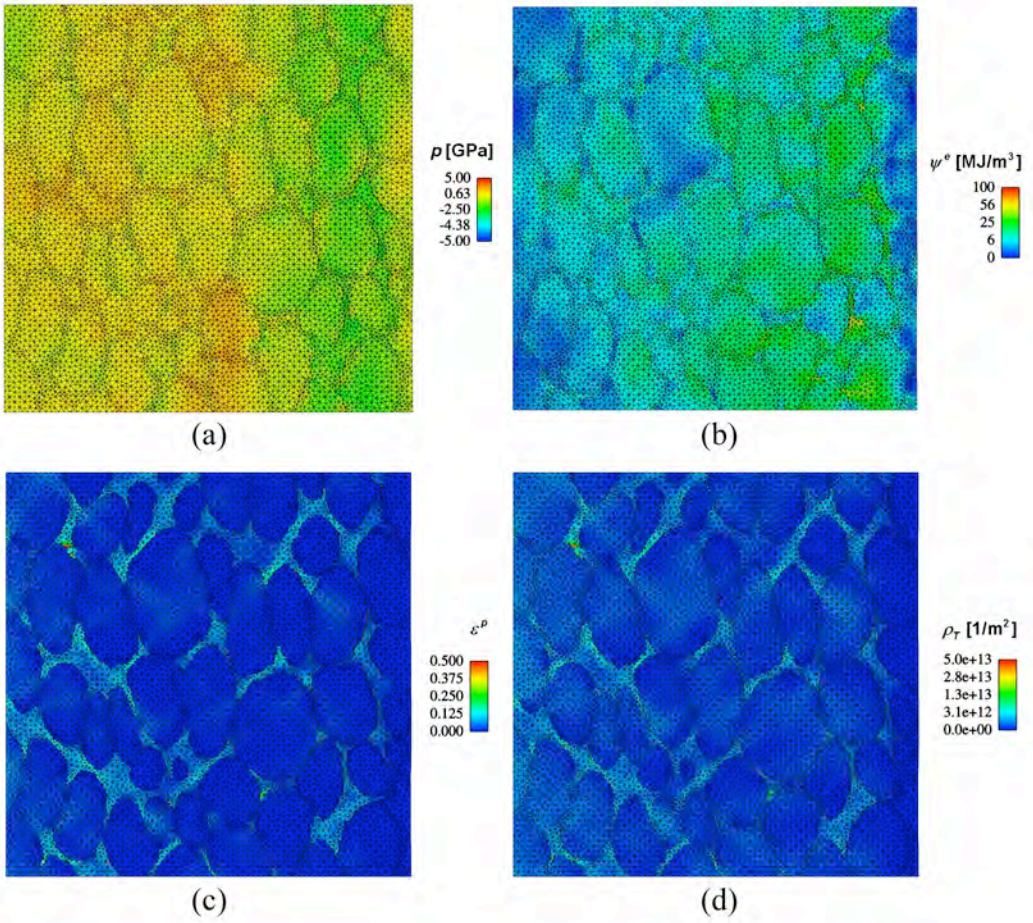
p [GPa]
5.00
0.63
-2.50
-4.38
-5.00
(a)
ψ^e [MJ/m^3]
100
56
25
6
0
(b)
ε^p
0.500
0.375
0.250
0.125
0.000
(c)
ρ_T [1/m^2]
5.0e+13
2.8e+13
1.3e+13
3.1e+12
0.0e+00
(d)

Figure 19

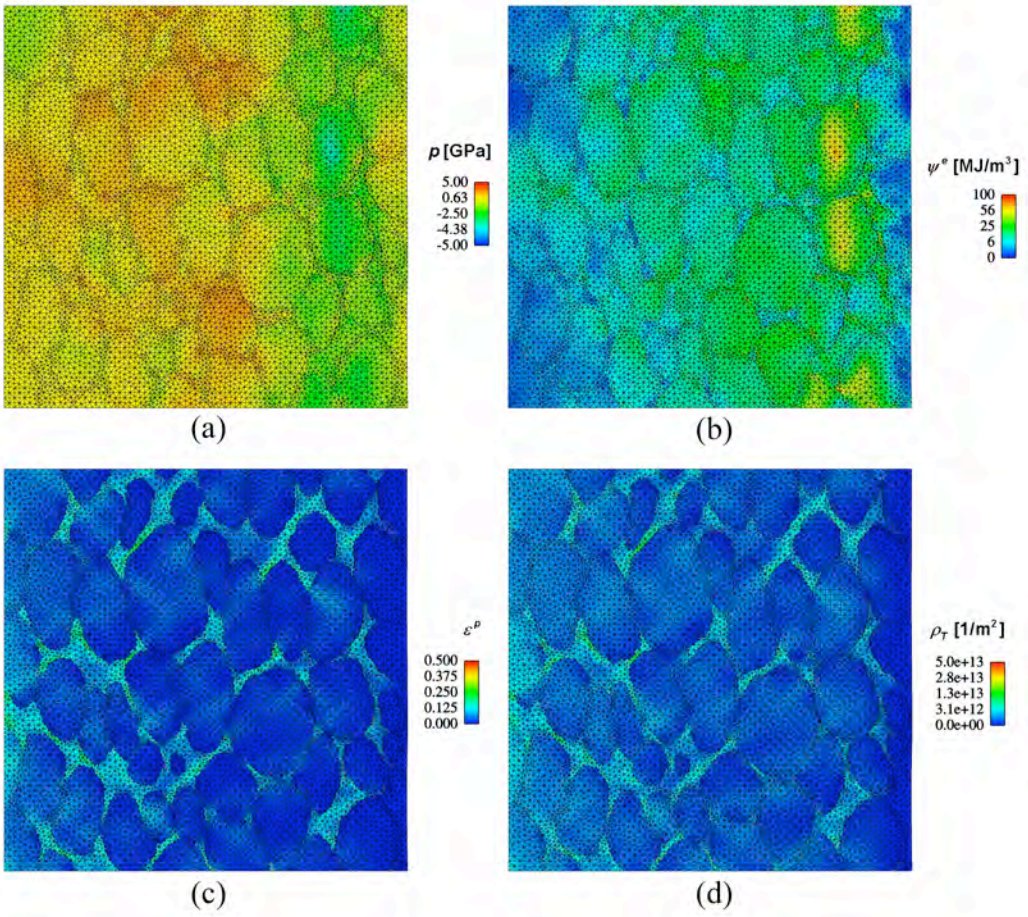
p [GPa]
5.00
0.63
-2.50
-4.38
-5.00
(a)
ψ^e [MJ/m^3]
100
56
25
6
0
(b)
ε^p
0.500
0.375
0.250
0.125
0.000
(c)
ρ_T [1/m^2]
5.0e+13
2.8e+13
1.3e+13
3.1e+12
0.0e+00
(d)

Figure 20

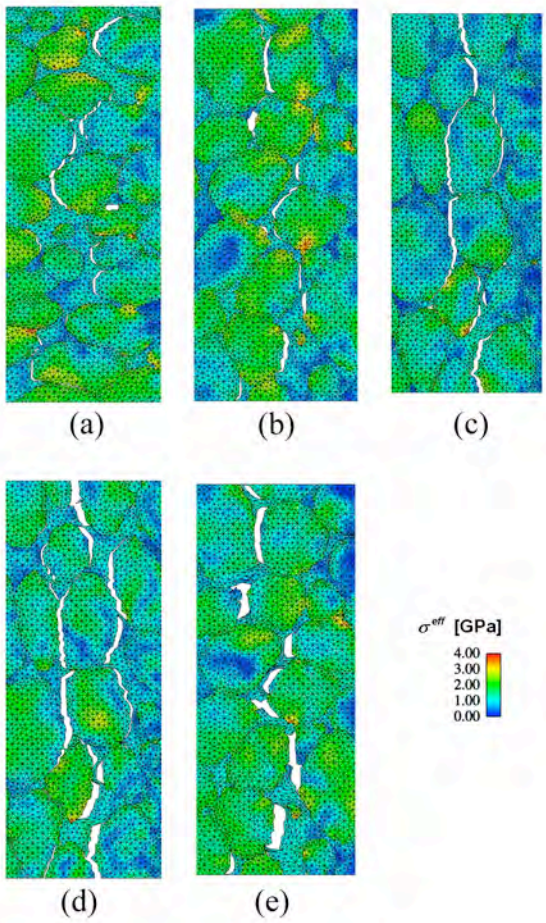

Figure 21

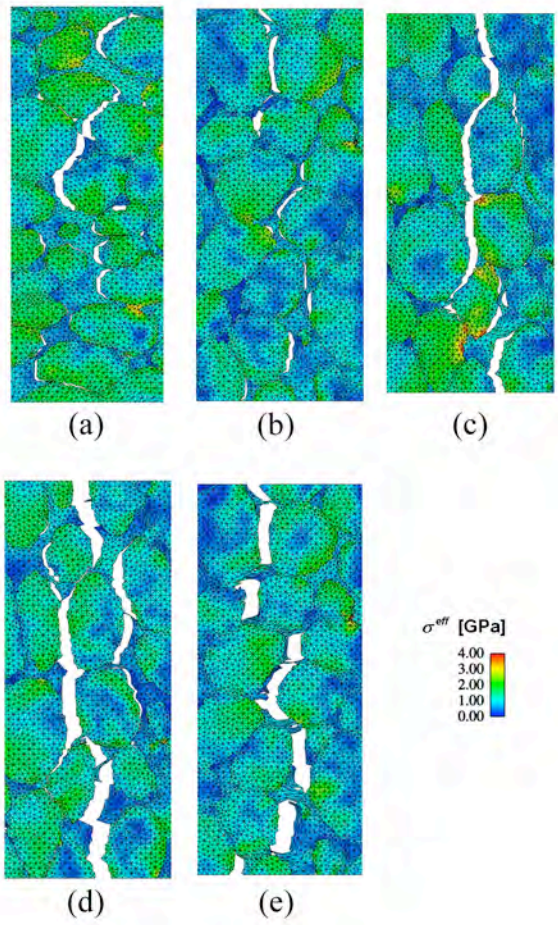

Figure 22

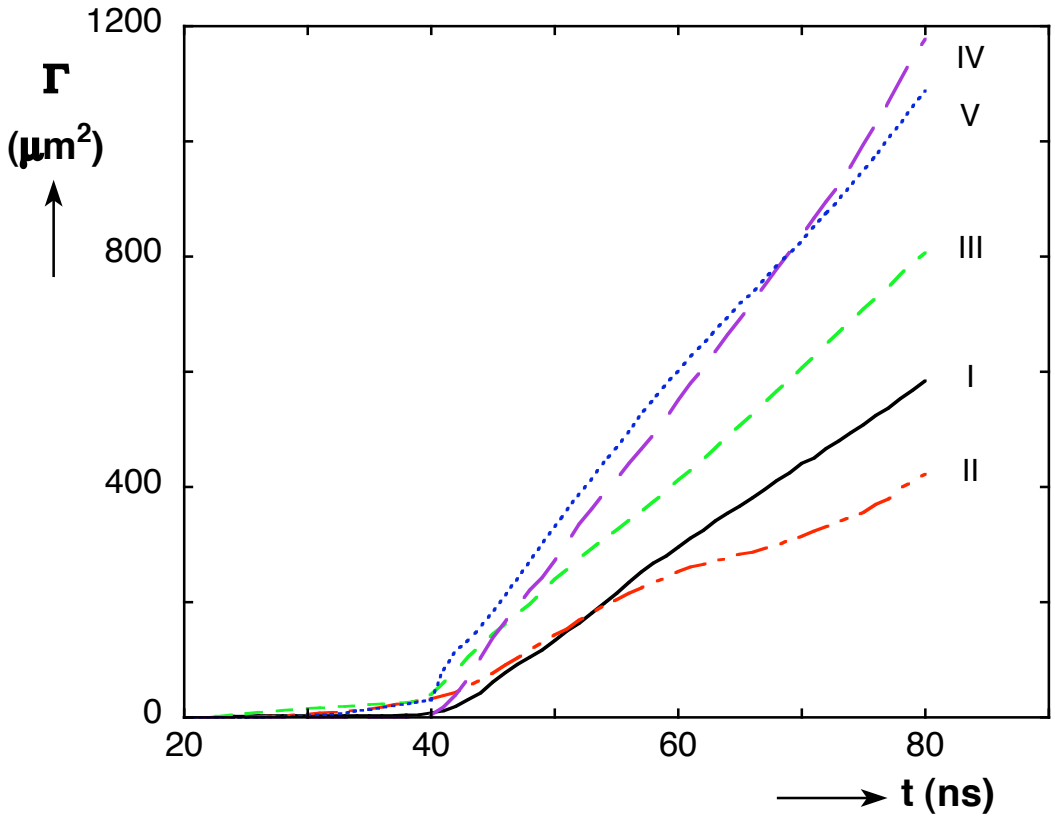
Γ
(μm²)
1200
800
400
0
20
40
60
80
t (ns)
IV
V
III
I
II

(a)

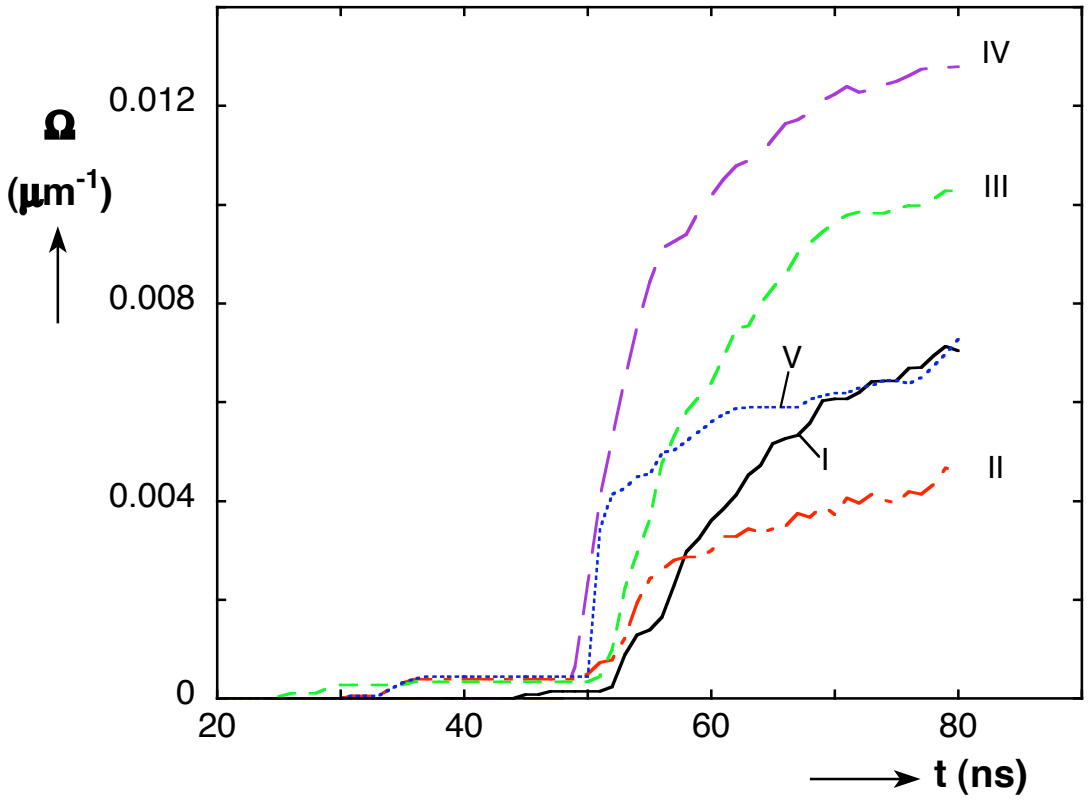
Ω
(μm⁻¹)
0.012
0.008
0.004
0
20
40
60
80
t (ns)
IV
III
V
I
II

(b)

Figure 23

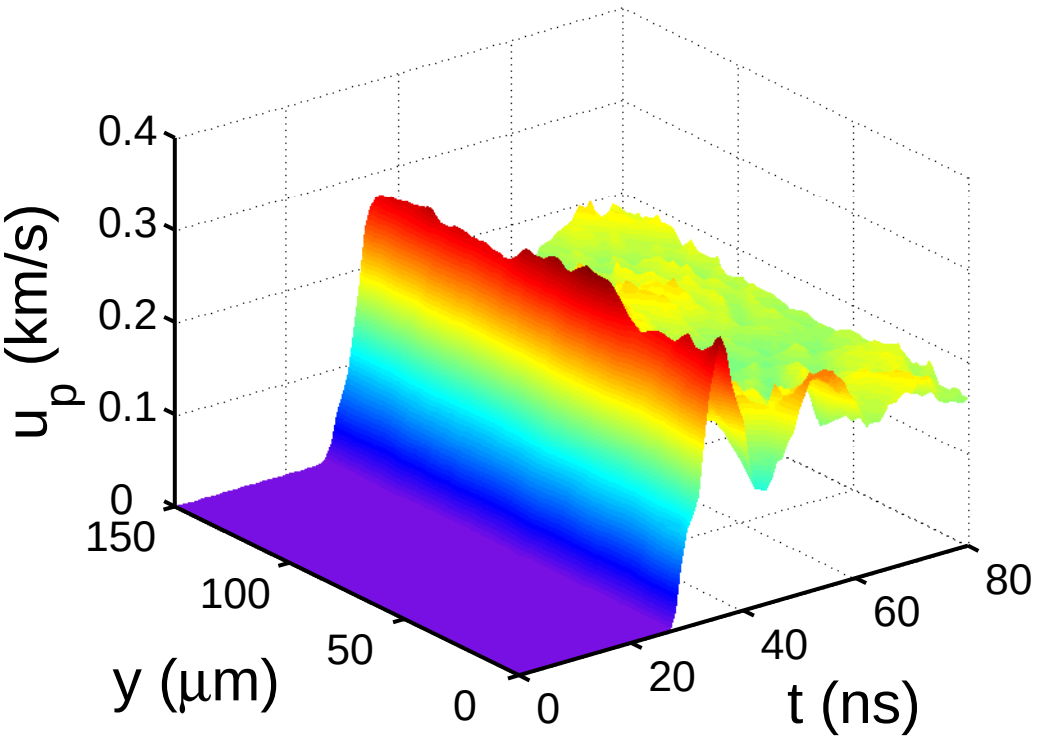

Figure 24

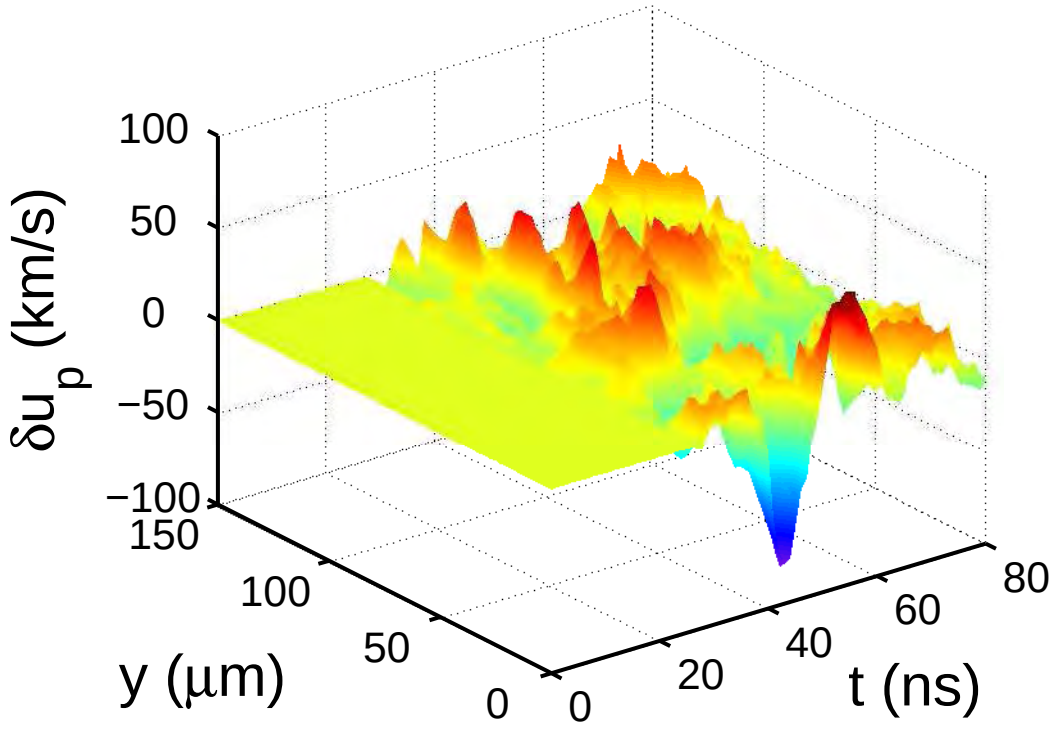

Figure 25

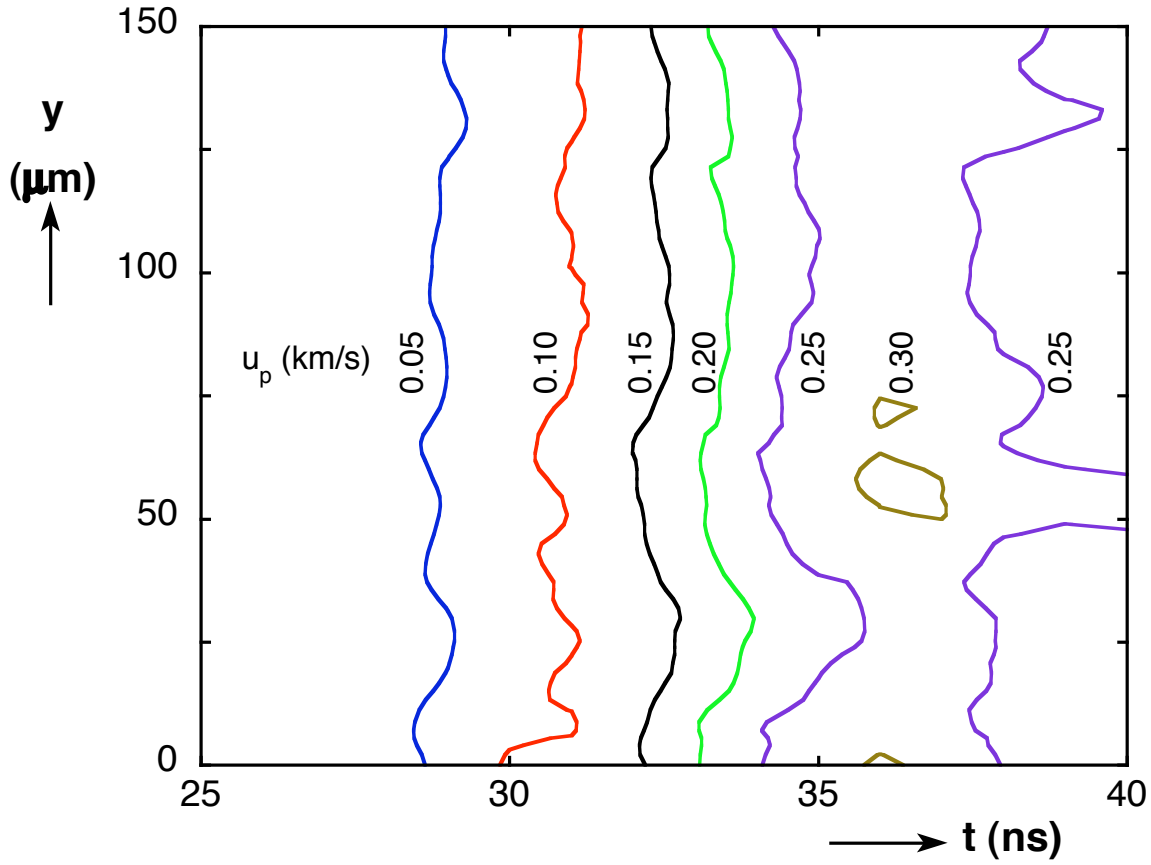

Figure 26

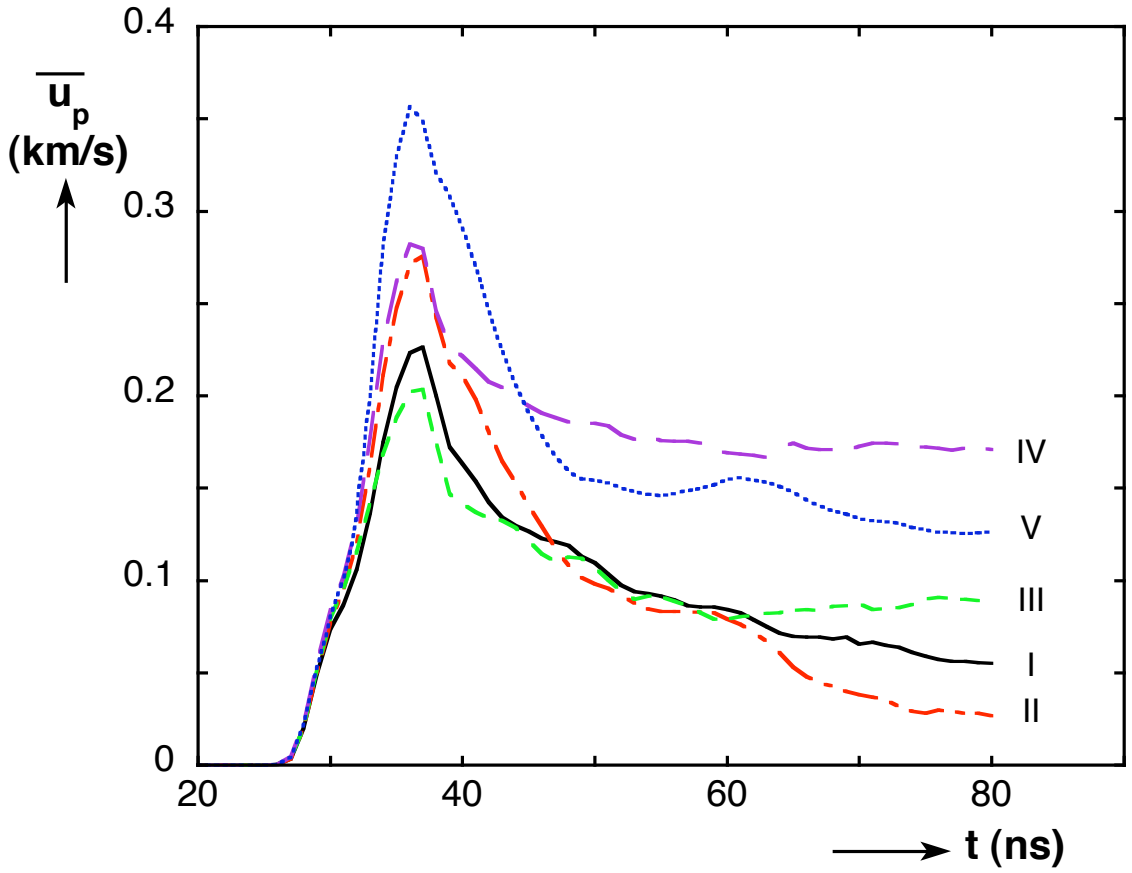

Figure 27

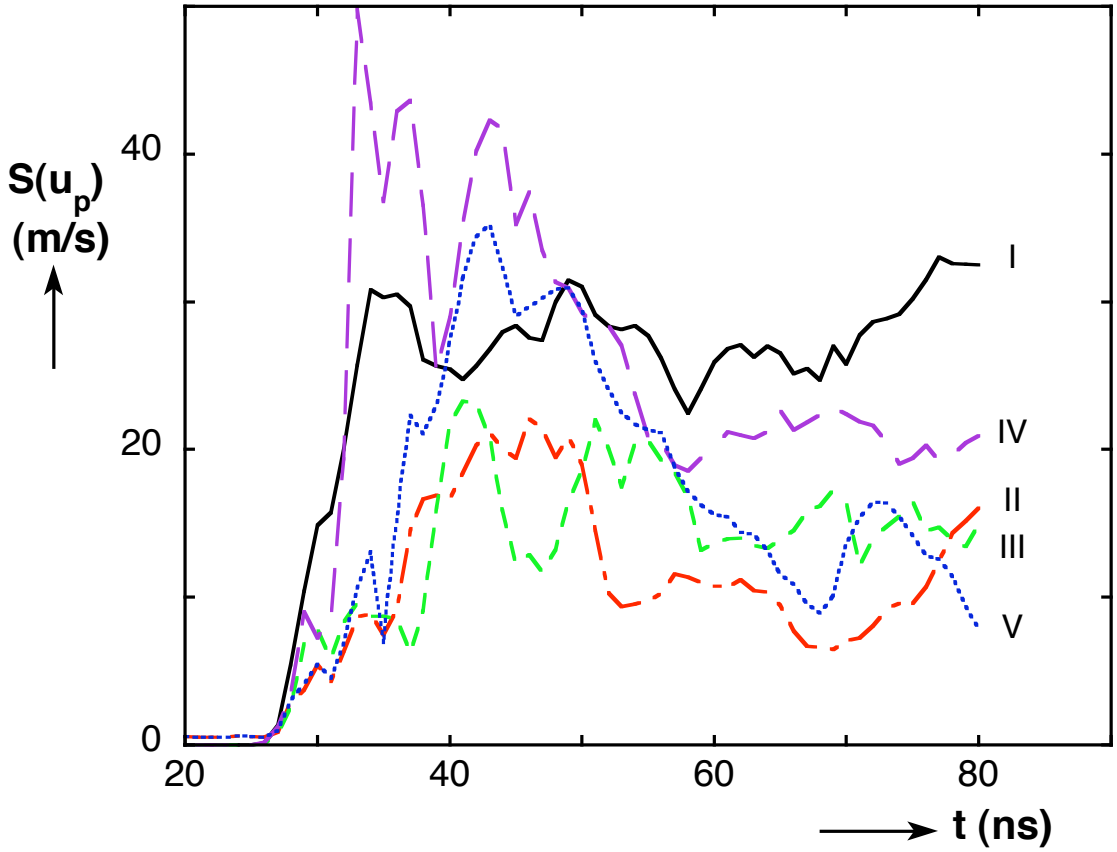

Figure 28

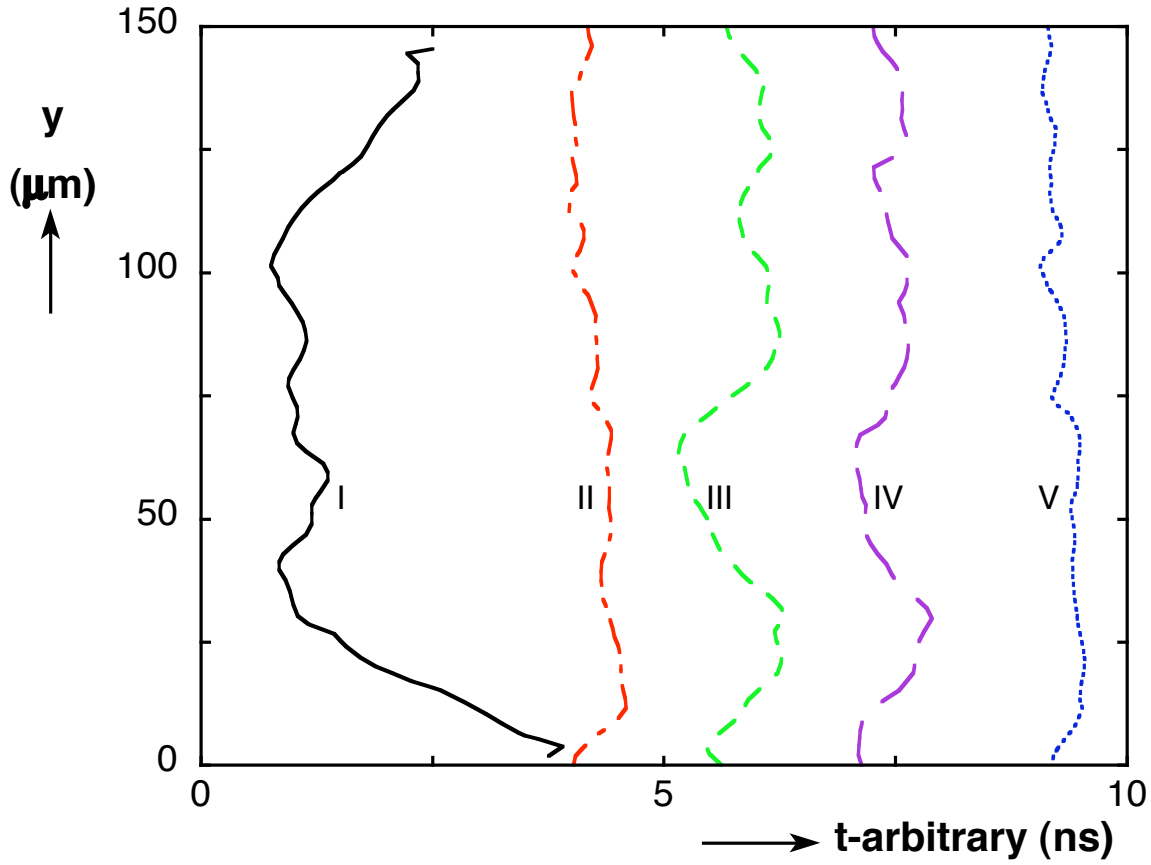

Figure 29

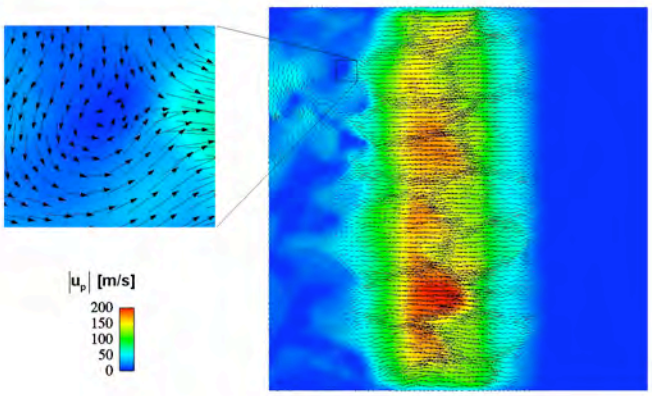

(a)

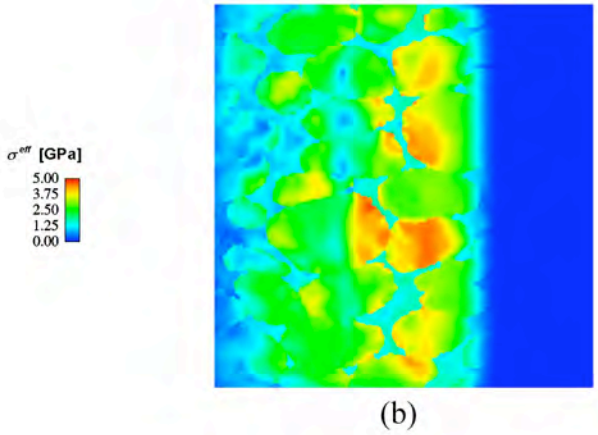

(b)

Figure 30

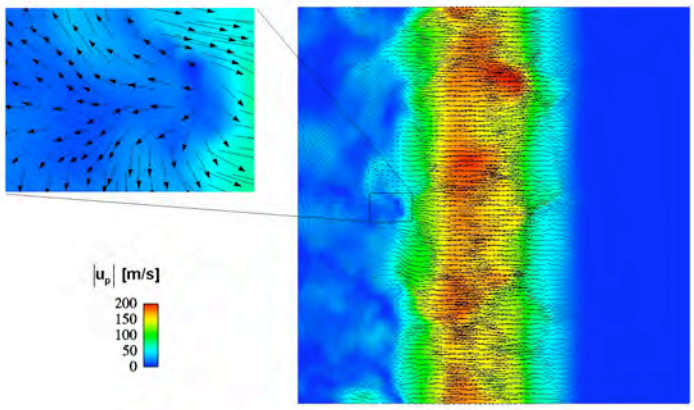

(a)

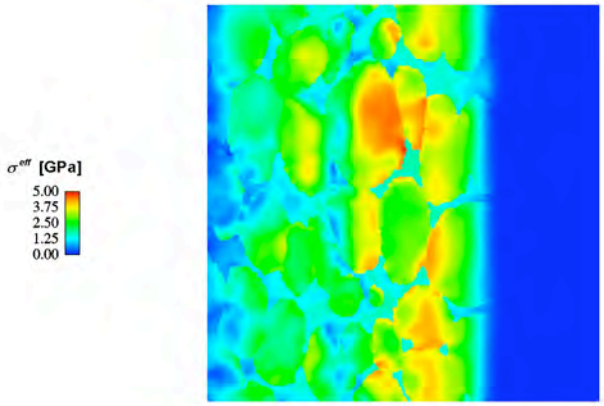

(b)